CORROSION BEHAVIOUR OF FRICTION STIR PROCESSED QE22 MAGNESIUM ALLOY

A DISSERTATION

Submitted in partial fulfilment of the

Requirements for the award of the degree

of

MASTER OF TECHNOLOGY

in

METALLURGICAL AND MATERIALS ENGINEERING

(With specialization in Materials Engineering)

By

ANKUR

DEPARTMENT OF METALLURGICAL AND MATERIALSENGINEERING

INDIAN INSTITUTE OF TECHNOLOGY ROORKEE

ROORKEE-247 667 (INDIA)

MAY, 2018

INDIAN INSTITUTE OF TECHNOLOGY ROORKEE

ROORKEE

CANDIDATE'S DECLERATION

I here by certify that the work which is being presented in this thesis entitled **"CORROSION BEHAVIOUR OF FRICTION STIR PROCESSED QE22 MAGNESIUM ALLOY"** in partial fulfilment of the requirements for the award of **Degree of Master of Technology** in **Metallurgical and material Engineering** with specialization in **Materials Engineering** and submitted in the Department of Metallurgical and Materials engineering of the Indian Institute of Technology Roorkee is an authentic record of my own work carried out during a period from June 2017 to May 2018 under the supervision of **Dr. G. P. Chaudhari** , Associate professor, Department of Metallurgical and Materials Engineering Indian Institute of Technology Roorkee.

The matter presented in this thesis has not been submitted by me for the award of any other degree of this or any other Institute

Date: Ankur

Place: Enrolment Number: 16545004

This is to certify that the above statement made by the candidate is correct to the best of my knowledge.

Dr. G. P. Chaudhari
Associate Professor
Department of Metallurgical and
Materials Engineering
Indian Institute of Technology Roorkee
Roorkee-247667

Date:

Place:

Acknowledgement

I wish to express my sincere thanks and gratitude to my supervisor Dr.G.P. Chaudhari, Associate Professor, Department of Metallurgical and Materials Engineering, Indian Institute of Technology Roorkee, for sharing his expertise at every stage of this project work without whose valuable guidance and constant encouragement this project would not have been possible. I owe a lot to him for showing a way out every time I hit a dead end and thought nothing could be done further. I thank him for all the moral support and patience which he showed during the course of this project

I would like to express my special sense of gratitude to Dr. Anjan Sil, Head of the department, Department of Metallurgical and Materials Engineering, Indian Institute of Technology Roorkee, Roorkee for his co-operation and inspirational support at all stages of my project as well as during this course of M.Tech.

I owe a particular thanks and gratitude to Dr. Amit Kumar Sen, Head of the Department, Institute Instrumentation Centre, Indian Institute of Technology Roorkee, Roorkee for extending selfless guidance each time I approached him. I am very grateful to him for his accessibility every time I needed a support and giving me a patient hearing about my problems. I am also thankful to him for his support in carrying out XPS analysis at his centre.

I take this opportunity to thanks all the faculty members of my department for their help and support which they rendered during this course and in the completion of this project. I would like to thank all the laboratory superintendents of this department who provided me support in the form of their expert opinions in the understanding of certain machines and logistics availability like polishing papers and certain chemicals.

I would like to extend my thanks to Mr. Nitin Panwar and Mr. Neeraj Srivastava, Research Scholar who gave me his valuable time to carry out corrosion experiments. He showed special interest by helping me in setting up the corrosion testing instrument and guided me in order to complete my experiments successfully. My sense of gratitude also goes to Mr. Rahul Gupta, Mr. Himanshu Kalra and Mr. Nitish Raja Research Scholars who took a keen interest in listening to my problems and guiding me towards a right direction.

In order to achieve one's goal in life, few sacrifices and constant prayers are must. I am grateful to Almighty to give me such parents who sacrificed their rightful comfort in nurturing me to reach a place where I am now and persistently praying for me and my success. I am extremely indebted to my parents and family members for their support, sacrifices and prayers without which this journey would not have been possible.

CONTENTS

List of Figures

List of Tables

Abstract

Effect of the microstructural changes after friction stir processing on the corrosion behaviour of rare earth added QE22 magnesium alloy is studied. The composition of QE22 alloy is 2.60 wt% Ag, 1.73 wt% Nd, and 0.68 wt% Zr, and balance magnesium. Its hardness varied from 90 VHN for FSP zone to 76 VHN for the base metal zone. Electrochemical tests performed in 3.5wt% NaCl solution showed that FSPed alloy with ultrafine grained magnesium matrix with dissolved ($Mg_{12}Nd_2Ag$) precipitates and refined second phase ($Mg_{12}Nd$) precipitates displays a significantly lower corrosion resistance. There are large number of micro-galvanic cells and it weakens the barrier to corrosion propagation in magnesium matrix. Higher weight loss is observed in immersion test, larger corrosion current values in polarization studies and lower charge transfer resistance and capacitance values in EIS plots. The inferior corrosion resistance of FSPed alloy is attributed to three factors. Firstly, deformation induced crystal defects made the magnesium matrix more active. Secondly, the refined second phase ($Mg_{12}Nd$) precipitates formed a large number of micro-galvanic cells and promoted corrosion in the magnesium matrix. Lastly the dissolution of continuous net like precipitates ($Mg_{12}Nd_2Ag$) in magnesium matrix promoted corrosion in FSPed alloy.

Chapter 1

Introduction

Magnesium is an eight most common element of our earth crust and third most abundant material [1]. Atomic number of magnesium is 12. It belongs to the alkaline earth metals of the periodic table. Its oxidation number is +2. It is highly soluble in water. Magnesium has a density of 1.738 g/cm^3 at 20°C which is almost one-fourth that of steel and two-third of aluminium. Magnesium does not exist in pure form due to its high reactivity. It exists in the form of (Mg^{2+}). Magnesium alloys are projected as structural metallic material for 21st century due to their high strength to weight ratio. Magnesium has an hcp structure. The lattice parameters of pure magnesium at 25 °C are a = 0.32092 nm and c = 0.52105 nm. The c/a ratio 1.6236, which makes magnesium nearly perfectly close-packed ($c/a = 1.633$) [2, 3].

According to the globally used designation of magnesium alloys the first letters indicate the major alloying elements and are followed by numbers which represent the elements in wt%. Magnesium and magnesium alloys have major applications in various places like electronics, transportation, biomedical, automotive field and aircraft industries [4]. By using magnesium alloys we can increase the vehicle fuel economy. Magnesium is a lightest structural material. Generally, aluminium, zinc, manganese, silicon, copper, rare earth, zirconium are added as an alloying elements in magnesium. Magnesium alloys may be either cast or wrought. But cast alloy magnesium alloys are more commonly used. Since 2003, wrought alloys are extensively used. The melting point of magnesium is approximately 923 K. It is highly flammable and reactive material. Due to their lower strength, ductility, and poor corrosion resistance their application is limited to specific areas [5]. Magnesium alloys exhibit some good properties such as high specific strength, castability suitable for high pressure die-casting, ability to be turned and milled at high speed under controlled atmosphere. But it exhibits some inferior properties like poor modulus of elasticity, low strength and low creep resistance at high temperature, high shrinkage allowances. However, due to its lightweight property, it is preferred choice in many places. Magnesium has a huge scope for use as biodegradable metallic implants in a cardiovascular and musculoskeletal application.

There are many ways to improve the mechanical properties, thermal stability at high temperature and corrosion resistance of magnesium alloys. Mechanical properties and corrosion resistance of magnesium alloy can be increase with grain size refinement and addition of rare earth element. In grain size refinement mechanical properties are improved according to the hall pitch relationship. There are many methods available to refine the grain size like.g. Equal channel angular processing, friction stir processing, rolling and burnishing. Equal channel angular processing is one of the most attractive and conventional methods of grain size refinement but it is a time-consuming. In addition, mechanical properties are improved due to the solid solution strengthening.

Grain refinement has some influence on the corrosion resistance of a material, which also depends on other morphological and topographical features. It is observed that smaller grain size can reduce the corrosion resistance of material. In some magnesium alloys like AZ61, AZ31B, and grain refinement improved the corrosion resistance but in other alloys like AZ91D alloy grain size refinement reduced the corrosion resistance. Pre and post heat treatment process in ultrafine grain magnesium alloy also affected the corrosion resistance. Lot of work has been done to reduce the drawbacks of magnesium and its exploit positive features. This led to the development of several groups of alloys. The alloy development has been guided by desire to improve-the following:

a) Specific strength

b) Ductility and density

c) Creep resistance

d) Corrosion resistance

a) Specific strength: In terms of specific strength, the most popular magnesium alloys are AZ and AM series alloys. In these alloys the main elements along with magnesium and aluminium are zinc (Z) and manganese (M). AM series alloys are generally suitable for die-casting applications, and AZ series alloys are suitable for wrought applications. Their success is due to the good combination of mechanical properties, workability, and castability [6].

b) Ductility and density: If we add lithium as an alloying element to magnesium alloys, it increases the ductility and reduces the density. Lead and tin also help to increase the ductility of magnesium alloys.

c) Creep resistance: Alloying of magnesium by thorium can withstand the highest temperature of 350^0C. But due to radioactive nature, it has only limited applications [7].

d) Corrosion resistance: Poor corrosion resistance of magnesium alloys is a major problem. Corrosion resistance of alloys depend on the grain size, internal stress, dislocation density, texture, solution composition, alloying element, and the second phase. The standard potential of magnesium (-2.375 V) is the most active potential of all structural materials [8].

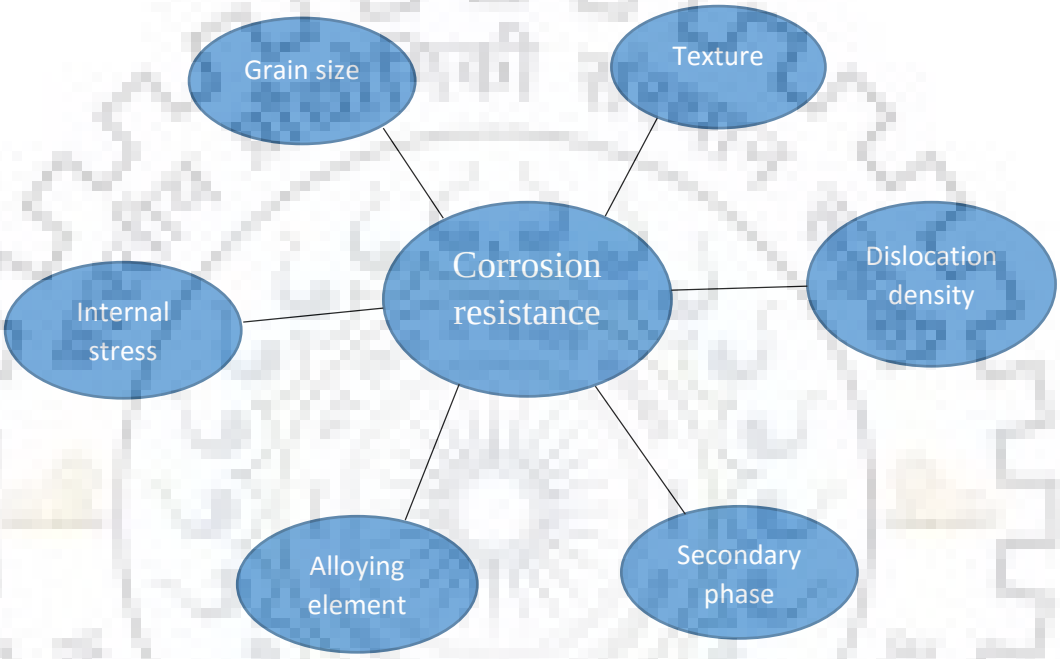

Figure 1. Factors affecting rate of corrosion.

Although, severe plastic deformation (SPD) processing of metals leads to significant improvement in mechanical properties, its effect on the corrosion resistance is not always favourable. It has been demonstrated that SPD processing of QE22 alloy leads to improved mechanical properties, however, its corrosion behaviour is not characterized in detail. Therefore, the objective of the present study are to evaluate the corrosion behaviour of friction stir processed QE22 (2.6 wt% Ag, 2.07 wt% Nd, 0.6 wt% Zr) alloy, and compare it with that of the base alloy. Corrosion studies are performed in 3.5 wt% NaCl solution to determine the effect of microstructure on corrosion properties.

Chapter 2

Deformation process and phase diagram of magnesium alloys.

2.1 Friction stir process

Friction stir processing (FSP) is a surface engineering technology that can refine the microstructures by surface modification, resulting in improved strength, ductility, fatigue, formability, and other properties. Ultra fined grains can be produce with the help of FSP up to a certain thickness. Non consumable larger diameter shoulder and profiled pin tool forcing into the surface of workpiece and travelling on the surface. By the help of appropriate tool design FSP process can be performed on larger area. Frictional heating and a large amount of deformation occurs during FSP causing the material to flow around the tool and consolidate in the tool's wake. FSP zones can be produced to depths of 0.5 to 50 mm. It is observed that for surface modification of non-ferrous alloy FSP has been used widely. Some advantages of FSP are (1) doubling the strength of cast aluminium and magnesium alloy (2) increased fatigue life.

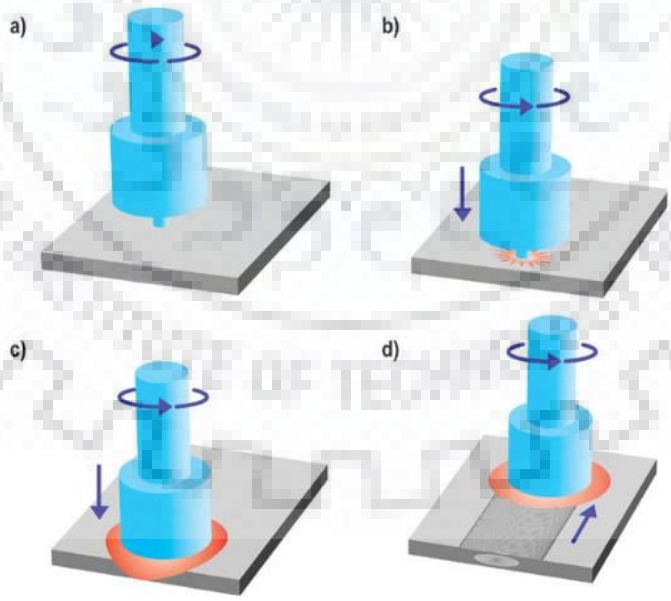

Figure 2. Schematic of friction stir process (a) rotation of tool before contact with the work surface, (b) small diameter pin contact with work surface, (c) shoulder contact with work surface, and (d) tool movement relative to the work surface [9].

A schematic illustration of FSP is shown in Figure 2. For friction stir processing within a plate or sheet, a specially designed cylindrical tool is rotated and plunged into the selected area. The tool has a small diameter pin with a concentric larger diameter shoulder. When the rotating pin comes in contact with material surface, heat is produced due to the friction that softens the small upper surface of the material. Tool shoulder and length of entry probe control the depth of penetration. When the shoulder contacts the metal surface, its rotation creates additional frictional heat and soften a larger cylindrical area of metal column around the inserted pin. During FSP, the non-consumable tool moves relative to the work surface with multiple passes, until the fine grains would not formed. Hot working action would be formed by continuous rotation of tool which softens the material in a narrow zone and simultaneously flow of material would take place from the leading edge to its trailing edge. However, FSP is a local thermo mechanical process that changes the local properties without affecting the properties of a bulk material. The variation of temperature and strain rate with tool rotation during friction stir process for different alloy is given in table 1.

Table 1: Variation of temperature and grain size with rpm used in FSP.

Composition	**Tool rotation in (rpm)**	**Grain size (µm)**	**Temperature(K)**
Al-8.9Zn-2.6Mg	400	0.68	583
Al-5.3Mg-0.5Mn	600	2.6	723
Al-5.3Mg-0.49Mn	400	0.7	573
Al-5.3Mg-0.49Mn-0.06Zr	400	2.2	748
Al-4.7Mg-0.35Sc	95	1.3	773
Al-5.6Mg-0.18Sc	95	1.7	773

2.2 Magnesium alloy

2.2.1 Magnesium-Neodymium system

Park and Wyman [10] and Drits et al. [11] observed that the solubility of Nd in Mg at 819 K eutectic temperature is 0.1wt % Nd as shown in Figure 3. Later, Joseph and Gschneider [12] investigated the solubility of Mg in α-Nd as 8.2 wt% Mg at the 824 K. Nayeb-Hashemi and Clark [13] developed the Mg-Nd binary phase diagram based on the data available in reported literature. According to their analysis, five intermetallic compounds, MgNd, Mg_2Nd, Mg_3Nd, $Mg_{41}Nd$ and $Mg_{12}Nd$ along with terminal solid solutions of Nd and Mg, Mg in α-Nd, and Mg in β-Nd exist in the Mg-Nd phase diagram. Afterwards, According to Delfino et al. [14] a metastable phase Mg_2Nd is detected only in quenched samples and mg-rich stable phase $Mg_{41}Nd_5$ has been found. Pahlman and Smith [15] found the vapour pressure of Mg in Mg-Nd alloys in the temperature range 650–930 K by the Knudsen effusion technique. Ogren et al. [16] obtained the enthalpy of formation of MgNd compound and carried out thermodynamic modelling on the Mg-Nd system. In their assessment, the intermediate compounds MgNd, Mg_2Nd, Mg_3Nd, and $Mg_{41}Nd_5$ were treated as stoichiometric compounds.

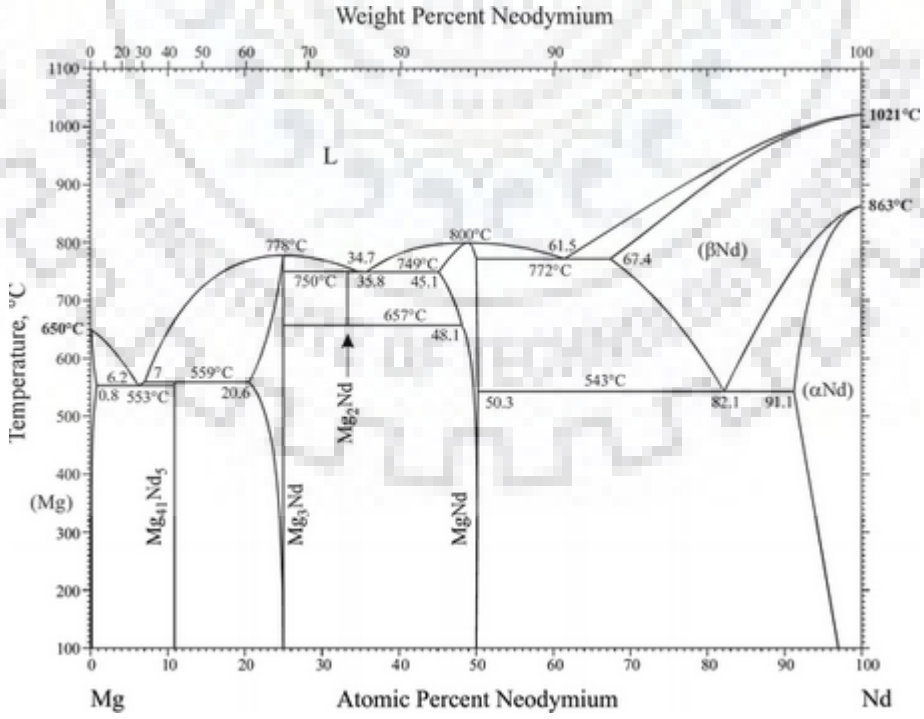

Figure 3. Mg-Nd equilibrium phase diagram [17].

2.2.2 Magnesium- Zirconium system

Solid solubility of zirconium in magnesium is also favoured because both the elements have a hcp crystal structure. However, magnesium exists in group II with a valency of 2, while zirconium is a transition element that exists in group IV with zero valency. As the valency between solvent and solute metals becomes more unequal, solid solutions become more restricted. Zirconium has an unfavourable valency for solid solution in a magnesium. A metal of lower valency tends to dissolve a metal of higher valency more readily and vice versa. This explains the low solubility of zirconium in magnesium and the high solubility of magnesium in zirconium. Zirconium is unique in that it is the only commercially significant transition element in groups III, IV, V, and VI used in magnesium-base alloys. More the electro positivity in solvent metal and more the electronegativity in solute metal, greater is the tendency to restrict solid solubility and form stable intermetallic compounds. The solubility of zirconium in magnesium is low and increases with temperature. In magnesium-zirconium phase diagram an alpha phase region has a maximum solubility of 0.87% of zirconium at 700°C. Adjacent to this zone a two-phase region containing magnesium-rich alpha solid solution plus zirconium-rich beta solid solution shown in Fig. 4. The structure becomes entirely beta when zirconium exceeds 30.3 wt%.

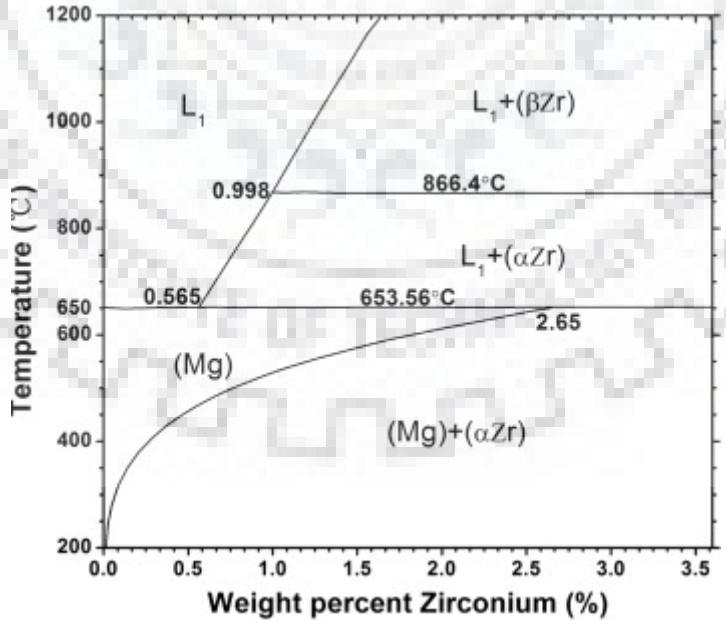

Figure 4. Mg-Zr equilibrium phase diagram [18].

2.2.3 Magnesium-Silver system

The maximum solid solubility of silver in magnesium is 4 wt% at 747K as shown in Fig. 5. The solubility of silver in magnesium varies with temperature. $AgMg_4$ intermetallic compound is formed at 80 wt% of magnesium. The $Ag_{17}Mg_{54}$ intermetallic compound is formed at 78 wt% of magnesium. Ag_3Mg (α') compound is formed between 10 wt% and 20 wt% below 665K. At low weight percentage of magnesium, the solubility of magnesium decreases with increasing temperature. An Intermediate solution of MgAg (β') is formed which has a higher melting point of 1098K.

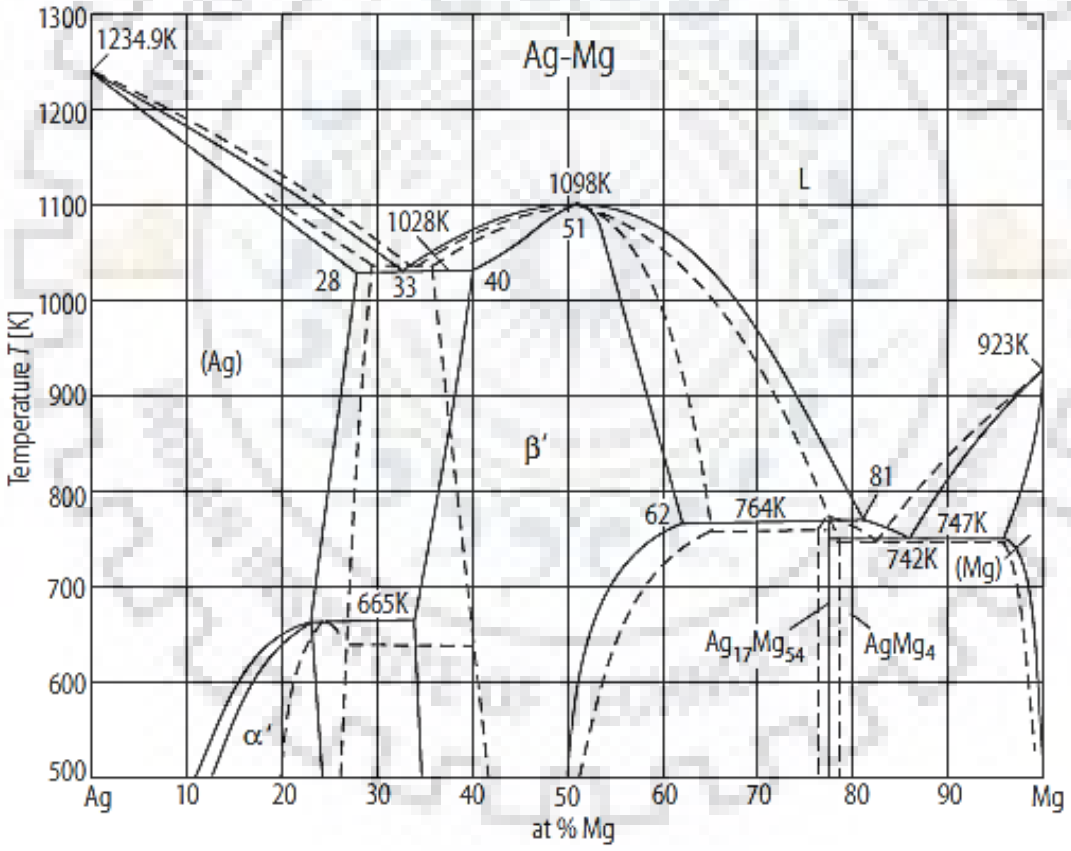

Figure 5. Mg-Ag phase diagram [19].

Chapter 3

Literature Review

3. Corrosion of severely deformed magnesium alloys

3.1. Galvanic corrosion

Galvanic corrosion is an electrochemical process in which two dissimilar metals are in contact with each other in the presence of electrolyte, out of which one metal acts as anode and other metal is acting as a cathode. Therefore, the material which behaves like an anode is corroded preferentially shown in Fig. 6. Similar galvanic reaction occurs in the cell for producing useful energy. There are many alloys in which more than one phase is corroded due to the galvanic effect. In this literature review, we will see in which magnesium alloy galvanic effect is responsible for corrosion.

The alloying elements in the magnesium always generate a second phase microstructure. Due to this, the susceptibility to galvanic corrosion increases. We know that magnesium itself is a very active metal. Generally, all the precipitates formed by alloying in magnesium have a high or nobler E_{corr} value.. Due to this when magnesium matrix encounters precipitates it corrodes preferentially. This is called as micro galvanic corrosion. Micro galvanic corrosion generally occurs due to the potential difference between magnesium matrix and second phase particles Song et al. [20] clearly demonstrate the galvanic corrosion in AZ91D magnesium alloy. The composition of AZ91D cast magnesium alloy was Mg-9wt%, Al-1wt% and Zn-0.206wt%, Fe-0.0029wt%, Cu-0.0416wt%, Si-0.0007wt%, Ni-0.0008%, Be- 0.0011wt%. The microstructure of AZ91D magnesium alloy consists of primary dendritic α-phase matrix with boundaries along which a continuous eutectic micro-constituent consisting of fine (α+β) phase in lamellar arrangement plus a coarse β-phase ($Mg_{17}Al_{12}$) along grain boundaries exists. Equal channel angular pressing is done in 1, 4, 8 and 12 passes to improve the mechanical properties of a material. During ECAP passes the fine β-phase particle is uniformly distributed in the α-phase matrix. β-phase is nobler than α-phase. Therefore, it acts as a cathode in the α-phase matrix. Due to this, a lot of micro galvanic cells are formed in the ECAP passed sample. Secondly, finer distribution of β-phase particle after ECAP reduce the barrier to retard the corrosion propagation in the α-phase matrix [21]. Therefore, the I_{corr} value of ECAP sample is more in

comparison to as received sample. The strain induced grain refinement increases the corrosion rate resulting in more pits and higher weight loss in immersion test done in NaCl solution. The large number of crystalline defects, high angle grain boundaries and dislocation offers α- phase matrix more corrosion activation and decreases the corrosion resistance of α-phase matrix.

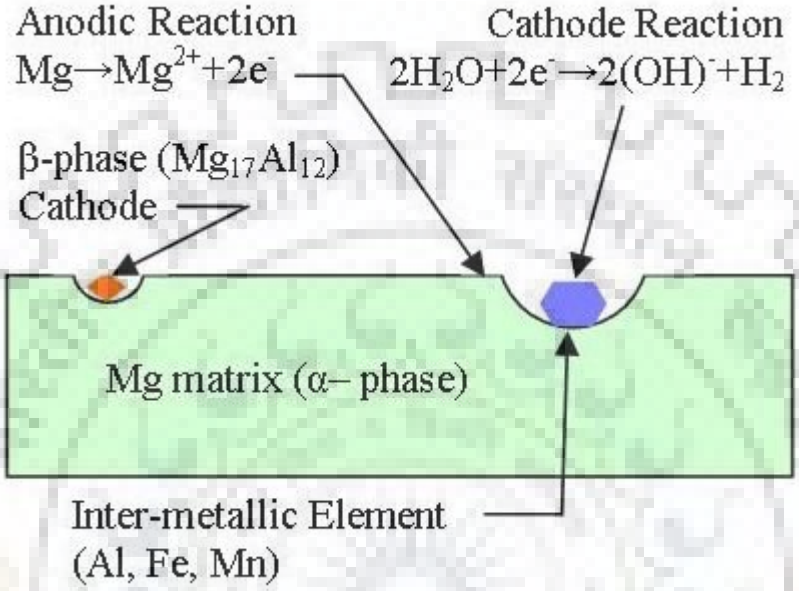

Figure 6. Galvanic corrosion between magnesium and secondary phase particles [22].

Galvanic corrosion rate depends onvarious factors such as the conductivity of the medium, potential difference between the anode and cathode, the area ratio of cathode and anode, and distance between the cathode and anode. Kim et al. [23] found the micro galvanic effect in an AZ61 alloy. The chemical composition of an AZ61 alloy used was 6.43 wt% Al, 1.09wt%Zn, 0.01wt%Mn, 0.01wt%Si, 0.001wt%Cu, 0.004wt%Fe, 0.001wt%Ni and rest was magnesium. This alloy consisted of nano sized particles of β-$Mg_{17}Al_{12}$ phase. Ultrafine grains are produced with the help of HRDSR. In AZ61 alloy weight loss in immersion test decreased with decrease in the grain size. It is observed that the weight loss in AZ61 alloy after HRDSR is 38.9 % lower than that of as-received sample. Due to severe plastic deformation of the material, area fraction of nano-sized β-phase particle is increased which provides a barrier to corrosion propagation. It is possible only due to the less spacing between the nano-sized β-phase particles. When a sample was annealed nano-sized β-phase distributed in a continuous manner along the grain

boundary and it acts as a barrier against the spread of corrosion. However, when the space between the nano-sizeds β-phase is large as in as received sample it forms a micro galvanic cell due to which the corrosion rate is increased. Finer distribution of nano-sized β- phase particles along the grain boundaries had low susceptibility to micro galvanic corrosion in the HRDSR-processed sample. So there is no any evidence of micro galvanic corrosion in processed sample. Coarse β- phase particles in without HRDSR- processed sample showed the evidence of micro galvanic corrosion. Thus, refining the β-phase particles into nano-sized structure reduces the susceptibility of micro galvanic corrosion between the α-phase matrix and the β-phase. Sometimes along with β-phase other intermetallic phases which consists of high amount of iron and magnesium work as cathode and form micro galvanic couples. Similarly when the precipitate is formed in the aluminium magnesium alloy, the concentration of aluminium in the eutectic precipitate is increased as compared to the α-matrix, which shows a different electrochemical behaviour and forms a galvanic cell. Pu et al. [24] illustrate the micro galvanic corrosion in AZ31B magnesium alloy. The composition of AZ31B alloy is 2.50wt%Al, 0.60wt%Zn, 0.20wt%Mn, 0.10wt%Si, 0.050wt%Cu, 0.040wt%Ca, 0.0050wt%Fe, 0.0050wt%Ni and rest is magnesium. The material is subjected to burnishing operation. It is a severe plastic deformation technique which can modify the surface structure. Due to the grain refinement in the material impurities are dissolved into the grain boundaries so less cathodic sites are available for galvanic reaction. Due to this the corrosion rate of material is decreased [25]. According to this study, grain size alone does not influence the corrosion resistance of material, but other factors like crystallographic orientation and residual stress are also responsible. A material having a smaller grain size but the lesser basal texture is less corrosion resistance as compared to the material having smaller grain size and strong basal texture.

3.2. Pitting corrosion

Pitting corrosion is defined as the removal of material from a small selected area when it comes in to contact with corrosive environment. This is shown in Fig. 7. Pitting corrosion depends on various microstructural features of materials like segregation, inclusion, and different phases. It also depends on the environmental conditions like oxygen concentration, chloride ion concentration, PH, flow rate etc. Naturally, magnesium is an active metal which undergoes a pitting corrosion at its corrosion potential E_{corr} when subjected to chloride ions under non-oxidizing environment [26]. In the presence of neutral and alkaline solution magnesium alloy surface is subjected to an aggressive attack of chloride ions which is responsible for pitting corrosion. So mostly, it is observed that pits always initiate adjacent to the second phase

particles. Song et al. illustrate that due to the breakdown of the passive layer pits initiate from the sides of second phase Al-Mg intermetallic particles. Sometimes high impurity level is also responsible for pitting corrosion. Arbegast et al. [27] observed the pitting corrosion in AM60 alloy which was exposed to sodium chloride solution. Initially, the surface was covered with a protective film. After the immersion in the sodium chloride solution, due to the aggressive attack of chloride ions breakdown potential of the protective film goes up to the value of corrosion potential of AM60 alloy which is equal to (-1.53V). Due to this the magnesium matrix around the intermetallic phase starts dissolving and forming a corrosion pit and corrosion product $Mg(OH)_2$ is produced with hydrogen gas.

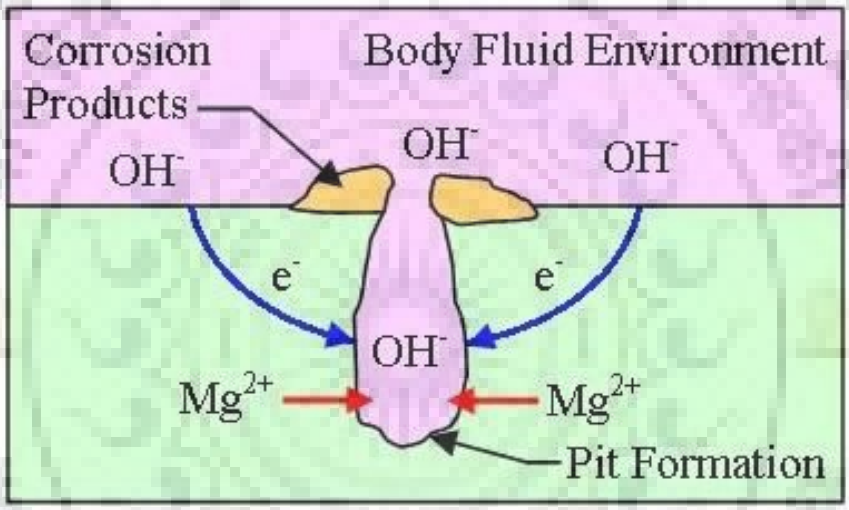

Figure 7. Pitting corrosion of magnesium in aqueous environment [28].

Pitting in a magnesium alloys follows an irregular path. It is not spread in vertically downward direction. It is spread in a lateral direction. Filiform corrosion is observed due to the galvanic action on the metal surface as the head of the track is anodic while the tail is cathodic. This type of corrosion is generally not seen in bare magnesium. It always initiates under the protective layer [29]. Hochet al. illustrate that initially, corrosion shows both types of localised corrosion- pitting as well as filiform corrosion.

Crevice corrosion is another type of localised corrosion. Crevice corrosion does not generally occur in magnesium alloy. While filiform corrosion is one of the special types of crevice corrosion and magnesium alloy can corrode due to the filiform corrosion. Now the question arises is why it does not corrode due to the crevice corrosion. Because crevice corrosion generally starts from a narrow gap its name is called crevice. Crevice

corrosion occurs due to the moisture contents which help corrode the metal surface. Ghali et al. [30] illustrate that crevice corrosion may start due to the hydrolysis of magnesium and magnesium alloy,which means oxygen is not required for the initiation of a crevice.

3.3 Inter-granular corrosion

In some cases, this type of corrosion is seen in magnesium alloys due to the precipitation of second phase particles along the grain boundaries as shown in Fig. 8. Grain boundaries are the most suitable site for precipitation and segregation. An alloy which has an intermetallic phase is more susceptible to inter-granular corrosion. Maker et al. [31] observed that inter-granular corrosion is normally not seen in magnesium alloys. In the magnesium alloy, second phase particles along the grain boundaries work as cathodes as compared to the magnesium matrix.

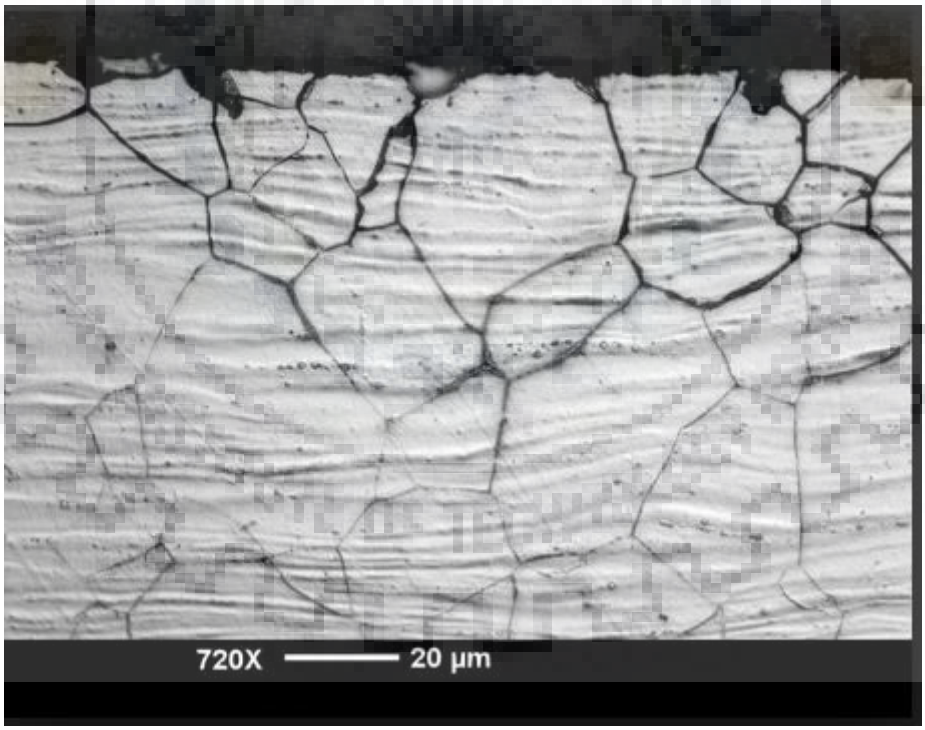

Figure 8. Schematic diagram of intergranular corrosion [32].

3.4. Stress corrosion cracking (SCC)

Stress corrosion is a phenomenon which occurs when the material is subjected to a tensile loading in a corrosive environment. It results in sudden failure of the material due to the growth of crack as shown in Fig. 9. In magnesium alloys, SCC generally does not occur along the grain boundaries. It mainly occurs across the grains, means that the transgranular type of fracture will take place. However, SCC can occurs along the grain boundary like in Mg-Al-Zn alloy due to the presence of $Mg_{17}Al_{12}$ precipitate along the grain boundaries. Speidel et al. [33] observed that alloying elements aluminium and zinc can increase the tendency of SCC. SCC in magnesium generally follows two mechanisms.

(1) Anodic dissolution of crack tip results in continuous propagation of the crack.

(2) Multiple fracture events at the crack tip results in discontinuous crack propagation.

The first model is also called dissolution model and the second model is called brittle fracture model. Loose et al. [34] observed that magnesium is highly resistant to SCC in alkaline medium. However, in neutral solution, there is a chance of SCC due to chloride contents.

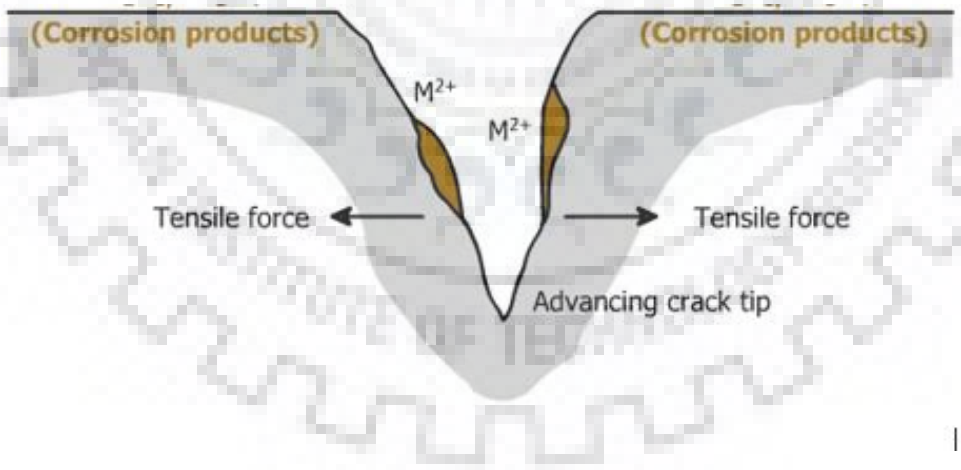

Figure 9. Stress corrosion cracking due to tensile force in corrosive environment [35].

3.5 Corrosion fatigue

Corrosion fatigue of magnesium alloys occurs due to cracks that propagate in a mixed trans-granular or inter-granular mode. Corrosion fatigue crack growth rate is accelerated in environments similar to those that accelerate SCC growth. The initiation and propagation of fatigue cracks is shown in Fig. 10. Experimental results showed a significant reduction in the fatigue strength in chloride containing solution. According to Stephens et al. [36] observed that the failure of AZ91-T6 material due to corrosion fatigue is more pronounced in aqueous solution in compare to air.

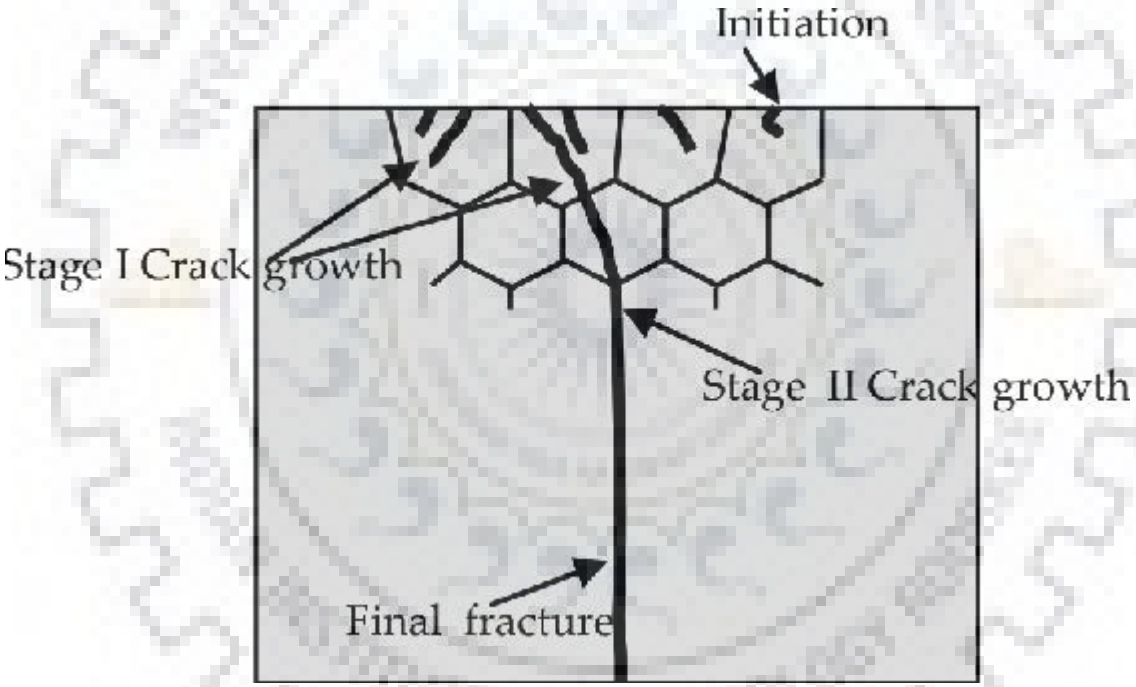

Figure 10. Initiation and propagation of fatigue cracks in corrosive environment [37].

Chapter 4

Characterization Technique

4.1 X-ray fluorescence technique

X-ray fluorescence (XRF) is the technique of emission of characteristic fluorescent radiation from the material that has been excited by bombarding with high-energy X-rays. This technique is widely used for elemental analysis and chemical analysis of metals, glass, and ceramics. When materials are subjected to short-wavelength X-rays ionization of atoms take place due to the ejection of one or more electrons. Ionization will take place if the atoms are exposed to radiation with energy greater than that of its ionization energy. Removal of an electron makes the electronic structure of the atom unstable, and electrons in higher energy shell fall into the lower energy shell in order to fill the hole left behind. This results in release of energy in the form of a photon. The energy of photon will be equal to the energy difference between the two orbitals involved.

4.2 Optical microscope

The optical microscope is referred as a light microscope that uses visible light and a system of lenses to magnify the images of small objects. Optical microscopes are the oldest technique to reveal the microscopic features. Optical microscope is very simple to operate although many complex designs aim to improve resolution and sample contrast. The microscopic features like grain size and precipitate size of as-received magnesium alloy was investigated under the light microscope. The principle of optical microscope includes the creation of a magnified image of an object specimen with an objective lens and the image is magnified furthermore with an eyepiece lens to allow the user to observe it with the help of naked eyes. However, the last image to be observed is an inverted virtual image. Microstructures of QE22 alloy were examined using a Leica DMI 5000 M optical microscope shown in Fig.11.

Figure 11. Leica DMI 5000 M optical microscope.

4.3 Scanning electron microscope (SEM)

SEM is one of the most widely used characterization methods for high resolution imaging and micro analysis for solid surfaces. Therefore, the study of microstructure using SEM is very much essential in order to understand the properties of the materials. SEM produces images of a sample by scanning the surface using a beam of high energy electrons. The high energy electrons after interacting with the sample produce characteristics X-rays, secondary electrons and back scattered electrons as a result of an elastic and inelastic collision and scattering giving information about phase structure and orientation of the sample, surface morphology and texture, and chemical composition etc. SEM can capture images of the sample with dimensions ranging from several microns to few nanometres. A schematic view of an SEM is shown in Fig. 12. Morphology, topography and characteristic of the microstructure of magnesium alloy before immersion test and after immersion test were investigated with SEM. EDS (energy dispersive spectroscopy) was used to investigate the composition of precipitate in as-received and friction stir processed (FSP) samples. Peaks matching with energy levels at which X-rays

are received are displayed in EDS spectrum. These peaks correspond uniquely to a particular element of the periodic table. The concentration of an element in second phase precipitate is inferred by the intensity of the peak obtained in the EDS spectrum. The weight percentage of an element in second phase precipitate was analysed using EDS. A QUANTA 200 FEG SEM was used in this work.

Figure 12. Schematic view of scanning electron microscope.

4.4 X-ray diffraction techniques (XRD)

Phase identification of corrosion products of magnesium alloy after immersion test was done by X-ray diffraction technique (XRD) shown in Fig.13. Cobalt was used as a target material for X-ray production. X-ray impinges on the material surface and is diffracted from a particular planes which satisfy the Braggs law. The detector detects diffracted rays and result is shown in the form of peaks. These peaks correspond uniquely to a particular element of the periodic table. The existence of any phases can be detected corresponding to the existence of peaks. The

concentration of phases can be inferred by the intensity of peaks obtained in XRD. A smartLab, Rigaku japan X-ray diffractometer was used in this work.

Figure 13. X-ray diffraction equipment.

4.5 X-ray photoelectron spectroscopy

X-ray photoelectron spectroscopy (XPS) is also known as electron spectroscopy. It is used for chemical analysis. It is a surface analysis technique. It provides a quantitative and chemical state information of the material surface being studied. It is shown in Fig.14. The average depth of analysis for an XPS measurement is approximately 5 nm. The principle involves the detection of photoelectron emitted by the target material when X-rays of sufficient energy to knock out the electrons are impinging on material surface. XPS was done on the surface of magnesium alloy after immersion test to know the chemistry of surfaces like the formation of oxides and their empirical formula. XPS principle involves the detection of binding energy of photoelectron coming out of the sample. Peaks of binding energy versus intensity correspond uniquely to a particular element of the periodic table. A PHI 5000 VersaProbe III XPS system was used.

Figure 14. Schematic diagram of X-ray photoelectron spectroscopy.

4.6 Transmission electron microscope (TEM)

Transmission electron microscopy (TEM) is a technique in which a beam of high velocity electrons is transmitted through a thin specimen to form an image. The thickness of specimen is in nm. An image is formed due to the interaction of high velocity electron with the sample as the beam is transmitted through the specimen. Resolution of a TEM is higher than that of the light microscope and SEM due to the smaller de Broglie wavelength of high velocity electrons. This enables the instrument to detect fine details of material even as small as a single column of atoms, which is thousands of times smaller than a resolvable object seen in a light microscope. TEM has a huge scope in the physical, chemical and biological sciences. Electron gun, image producing and recording system are the essential components of a TEM. Besides the conventional transmission electron microscopy (CTEM), TEM can also appear in other forms such as scanning transmission electron microscope (STEM) and high-resolution transmission electron microscope (HRTEM). CTEM, STEM contains only a gun, an electron spectrometer & detection system and a probe-forming lens. TEM generally requires a very thin sample which can ensure the transmission of electrons and interaction with atoms either elastically or in elastically. Hence, sample preparation techniques such as ion beam milling and twin jet polishing are very much essential. Based on diffraction contrast different image modes

like bright-field and dark-field of TEM can be achieved. Microstructure investigation of magnesium alloy was done by transmission electron microscope which is shown in Fig. 15.

Figure 15. Transmission electron microscope.

Chapter 5

Electrochemical Measurement Techniques

Corrosion phenomena involve electrochemical reactions and thus the corrosion properties of the samples can be ascertained by studying those electrochemical reactions. Measuring current-potential relations in the controlled environment can provide valuable information of corrosion potentials, corrosion rates, behaviour and kinetics of the corrosion of specimen and many other important data. In the present study, the corrosion characteristics of as-received and severely deformed QE22 alloy was measured by three methods as mentioned below.

(a) Open circuit potential (OCP) measurement

(b) Potentiodynamic polarization technique

(c) Electrochemical impedance spectroscopy (EIS)

5.1 Open circuit potential (OCP)

The potential measured without the application of current or voltage in the electrochemical cell with respect to the reference electrode is called open circuit potential of the working electrode. In most corrosion experiments, OCP is measured first. In order to obtain considerably accurate results, OCP should be measured and sufficient time is allowed to stabilize the OCP before commencing the electrochemical measurements. A stabilized OCP indicates that the system which is being studied has attained a steady state in which various corrosion reactions have achieved equilibrium. OCP measurement is always followed by various electrochemical experiments as it is a qualitative measurement and it cannot quantify the corrosion rates. In the present study, corrosion rates of as-received and FSPed QE22 alloy are quantified with the help of potentiodynamic polarization technique.

5.2 Potentiodynamic polarization method

Potentiodynamic polarization method is used for the corrosion characterization of as-received and FSPed sample from current-potential relationship. The potential of a specimen is scanned in both positive and negative direction of the open circuit potential (OCP) and the corresponding anodic and cathodic currents are measured and plotted by means of the software. The measurements from the plot are used to determine corrosion behaviour of as-received and FSPed sample in the corrosive environment. This technique can also be used to investigate the effects of oxidizers and other corrosive environments on the specimen. Using this technique corrosion behaviour of specimens with various modified microstructures can be compared and an optimum condition can be examined based on the corrosion experiment results.

Usually current is plotted in logarithmic function with respect to the potential on a semi-log chart. The plot thus obtained is called potentiodynamic polarization curve [38]. Using Tafel's extrapolation method, various corrosion parameters of as-received and FSPed QE22 magnesium alloy in the corrosive environment are evaluated. The parameters include E_{Corr}, I_{Corr} and Tafel constants.

5.3 Electrochemical Impedance Spectroscopy (EIS)

EISis an electrochemical measurement technique. It is a frequency domain measurement made by applying a sinusoidal perturbation. EIS uses a small perturbations. These small deviations from equilibrium potential are assumed to have a linear response. EIS is performed by sweeping a wide range of frequencies at a single perturbation amplitude. Frequency ranging from 10 KHz to 10 mHz are generally used. Impedance is defined as the opposition to the flow of electric current having units of Ohms, Ω. It is a function of frequency. Interpretation of EIS data do based on models containing Equivalent Electrical Circuit (EEC) elements. Equivalent circuit has combinations of circuit elements such as resistors, capacitors, and inductors. These elements are attributed the physical processes in the system (e.g. double layer capacitance, charge transfer resistance, polarization resistance). In Nyquist Plot data from each frequency point is plotted between the imaginary part on the ordinate and the real part on the abscissa. The high-frequency intercept of Nyquist plot corresponds to the electrolyte resistance (R_s) or the ohmic resistance of the electrolyte. The low-frequency intercept corresponds to a

combination of electrolyte resistance and polarization resistance (R_s+R_p). Therefore, diameter of a Nyquist plot gives the value of polarization resistance.

Chapter 6

Experimental Procedure

6.1 Friction stir processing

The composition of 6 mm thick plate of a wrought QE22 alloy is 2.60 wt% Ag, 1.73 wt% Nd, and 0.68 wt% Zr, and balance magnesium. FSP was done in two passes with tool rotation of 800 rpm followed by 600 rpm at a feed rate of 100 mm/min. FSP tool had a shoulder diameter of 12 mm and a taper-threaded pin was 3.4 mm long with 6 mm root diameter.

6.2 Vickers micro hardness test

Vickers hardness test is easier to use as compared to other hardness tests. The required calculations in Vickers hardness tests are independent of the size of the indenter, generally, pyramid shape diamond indenter is used to measure the hardness of materials. The Vickers hardness test can be used for all the materials and has one of the widest scales among all hardness tests. The unit of hardness given by the test is known as the Vickers Pyramid Number (HV) or Diamond Pyramid Hardness (DPH). The hardness number is determined by load over the surface area of the indentation and not the area normal to the force. Vickers micro hardness tests were performed on FSP nugget zone and base metal zone in QE22 alloy using MVH-11 tester shown in Fig.16 to investigate the variation in hardness.

Figure 16. Vickers micro hardness tester.

6.3 Open Circuit Potential (OCP)

Magnesium alloy of rectangular shape having 1 cm^2 area was the working electrode, saturated calomel electrode (SCE) was the reference electrode and graphite was the counter electrode. Tests were performed for a duration of 48h with a sampling rate of 0.5/s. Tests were performed on the nugget portion of the FSPed sample and the base material. The standard flat Gamry electrochemical cell was used. The picture of the potentiostat/galvanostat is shown in Fig.17.

Figure 17. PAR 273A galvanostat/potentiostat.

The instrument is capable of controlling accurate current potentials in all electrochemical cells. The potentiostat responds rapidly to transitions in the form of steps in both potentiostatic and galvanostatic mode. The potentiostat is attached with a computer with Windows 98 as an operating system as the GPIB interface between the potentiostat. The potentiostat is programmed using Powersuite® software. All the electrochemical analysis is done using the same software with its modules such as Powercorr for potentiodynamic polarization curves. The electrochemical cell consisted of graphite as a counter electrode and SCE with lugging probe as a reference electrode. Fig. 18 shows the electrochemical cell used.

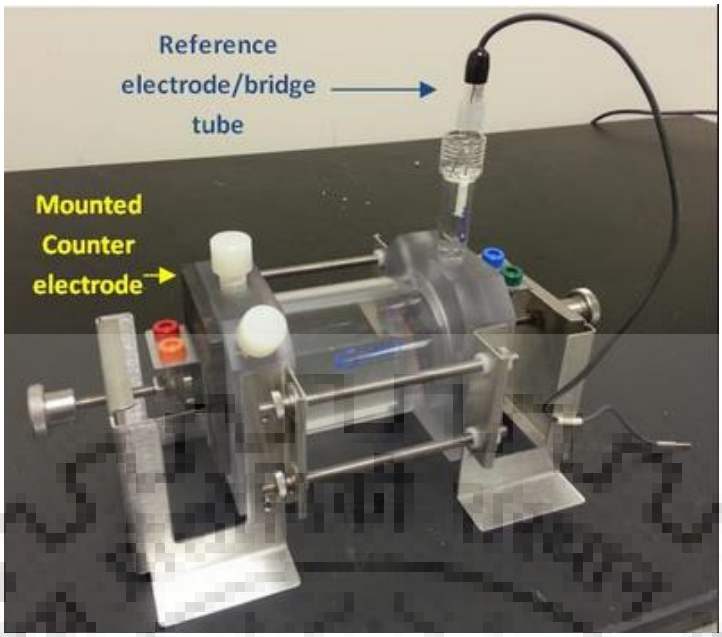

Figure 18. Photograph of the electrochemical cell.

6.4 Potentiodynamic polarization

Bath of 3.5wt% NaCl solution was prepared using distilled water. The pH of the solution is measured and recorded at the beginning of each experiment. The potentiodynamic polarization curves were obtained with potential ranging from -250 mV to 250 mV with respect to SCE with a sweep rate of 0.5 mV/s. Samples were cleaned with ethanol before testing. The samples were conditioned for 1 h for initial stabilization. Tests were performed in room temperature. All the tests were performed on the top surface of a nugget portion in an FSPed sample and repeated by three times in order to get reliable results.

6.5 Specimen preparation and etchant solution

For potentiodynamic polarization tests, 3.5 wt% NaCl solution was used to identify the effect of FSP on the magnesium alloy. Rectangular specimens of exposed area 1 cm^2 were used for determination of corrosion rate in both as-received and FSPed samples. For electrochemical tests and optical microscopy, samples were first mechanically polished to achieve mirror like finish by using successively finer grades of 320, 800, 1200, 1500 and 2000 grit emery papers and fine cloth polishing using diamond paste. The disc polisher is shown in Fig. 19. Samples

were cleaned with ethanol before testing. For immersion tests specimen were polished with 600 grit size emery paper followed by cleaning with ethanol. After immersion tests, the corrosion products were removed with chromic acid solution whose composition is given in Table 2. This was followed by washing with distilled water and drying. The composition of etchant solution used for optical microscopy are given in Table 3.

Table 2: Composition of chromic acid solution used for remove the corrosion product.

Chemical	**Concentration**
Chromium oxide	10 gram
Silver nitrite	1 gram
Distilled water	400 ml

Table 3: Composition of etchant solution

Chemical	**Concentration**
Picric acid	4 gram
Ethanol	70 ml
Acetic acid	10 ml
Distilled water	10 ml

Figure 19. Schematic of polishing machine.

Chapter 7

Results and Discussions

7.1 Microstructure

Fig. 20 and 21 (a) show the optical and SEM microstructures of as received QE22 alloy sample whose average grain size is 50±10 µm. Linear intercept method was used to determine the grain size of as-received sample. Fig. 21 (a) and (b) show the composition of precipitate in atomic percentage and weight percentage for both as-received and FSPed sample. Fig. 21 (a) corresponds to point A in the as-received sample. Fig. 21 (b) corresponds to point B in the FSPed sample. Alloy consists of $Mg_{12}Nd$ eutectic network along the grain boundaries and at the triple junctions of magnesium matrix. The average size of $Mg_{12}Nd$ eutectic after FSP measured using ImageJ software is 8±1.2 µm. Fig. 22 (a) corresponding to the cross section of a specimen shows that FSP has refined the grain size significantly due to severe plastic deformation (SPD). The morphology of $Mg_{12}Nd$ drastically changed from elongated to the globular. There is a significant decrease in the size of $Mg_{12}Nd$ after two passes due to which the surface area of second phase precipitate is increased. Fig. 22 (b) shows uniform distribution of $Mg_{12}Nd_2Ag$ precipitate in as-received QE22 alloy. Fig. 22 (c) shows the dissolution of $Mg_{12}Nd_2Ag$ precipitate after the FSP process. Fig. 23 (a) and (b) show the distribution of alloying elements in both as-received and FSPed samples.

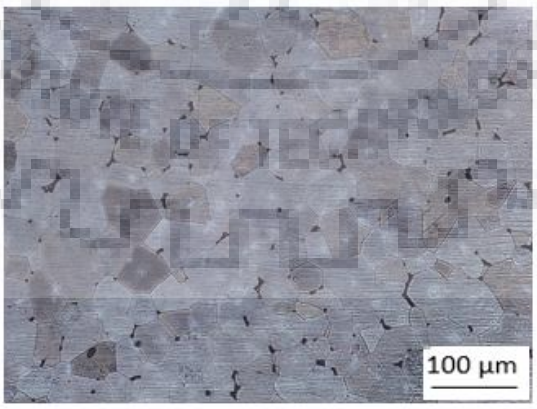

Figure 20. Optical micrograph of as received QE22 alloy showing equiaxed microstructure.

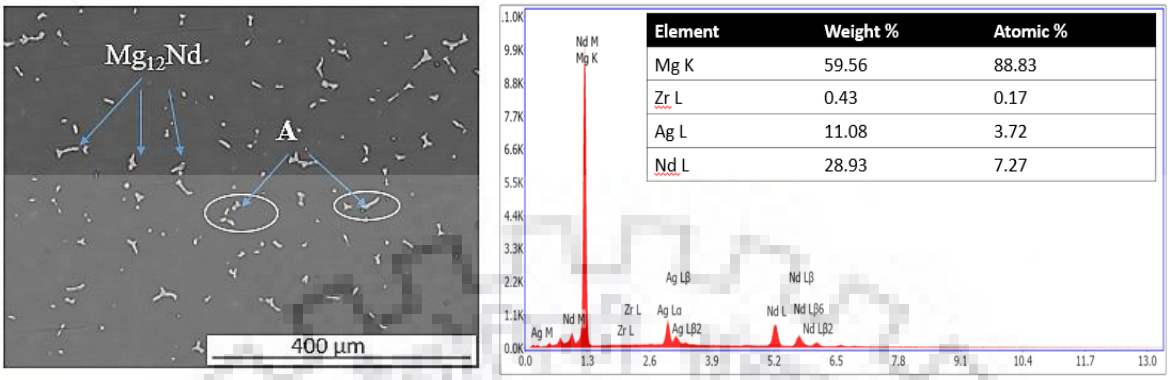

Element	Weight %	Atomic %
Mg K	59.56	88.83
Zr L	0.43	0.17
Ag L	11.08	3.72
Nd L	28.93	7.27

(a)

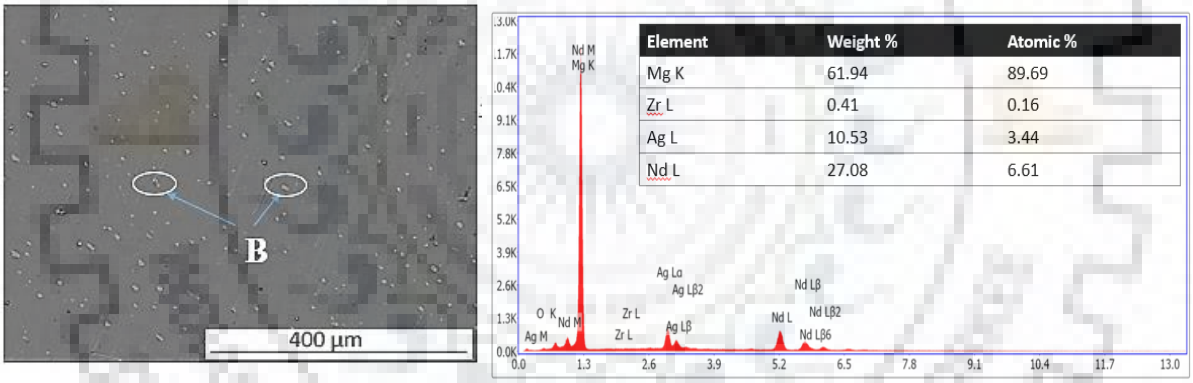

Element	Weight %	Atomic %
Mg K	61.94	89.69
Zr L	0.41	0.16
Ag L	10.53	3.44
Nd L	27.08	6.61

(b)

Figure 21. (a) SEM micrograph of as-received QE22 alloy with EDX pattern of minor phase. (b) SEM micrograph of QE22 alloy after friction stir process with EDX pattern of minor phase.

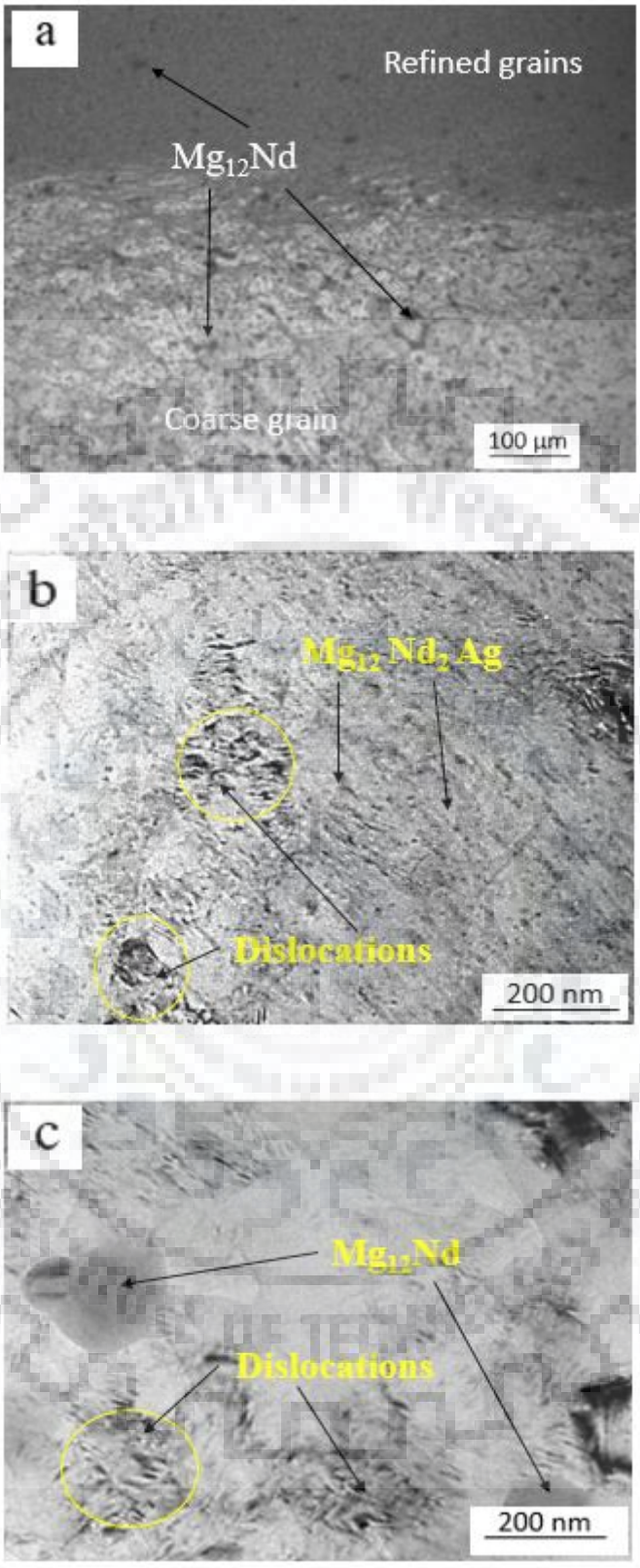

Figure 22. (a) Optical image of cross section of FSPed specimen, TEM images of (b) as-received, and (c) FSPed QE22 alloy.

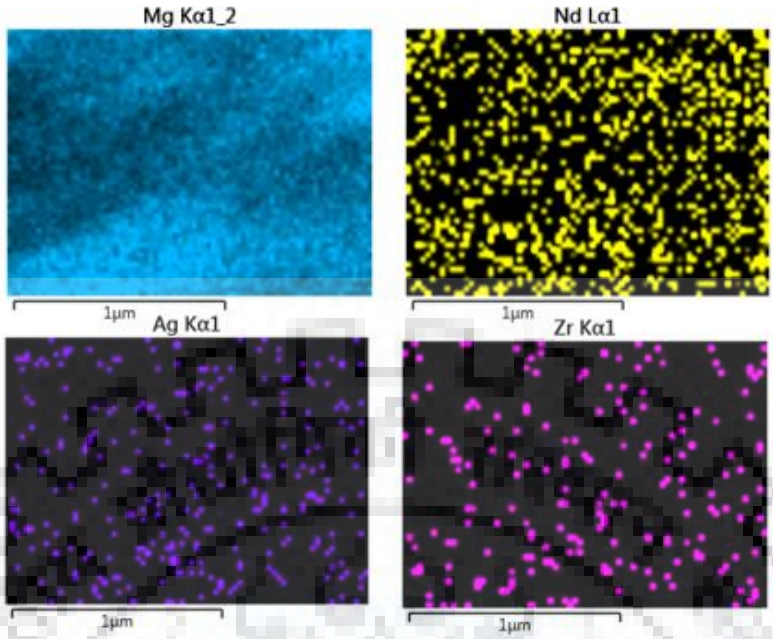

(a)

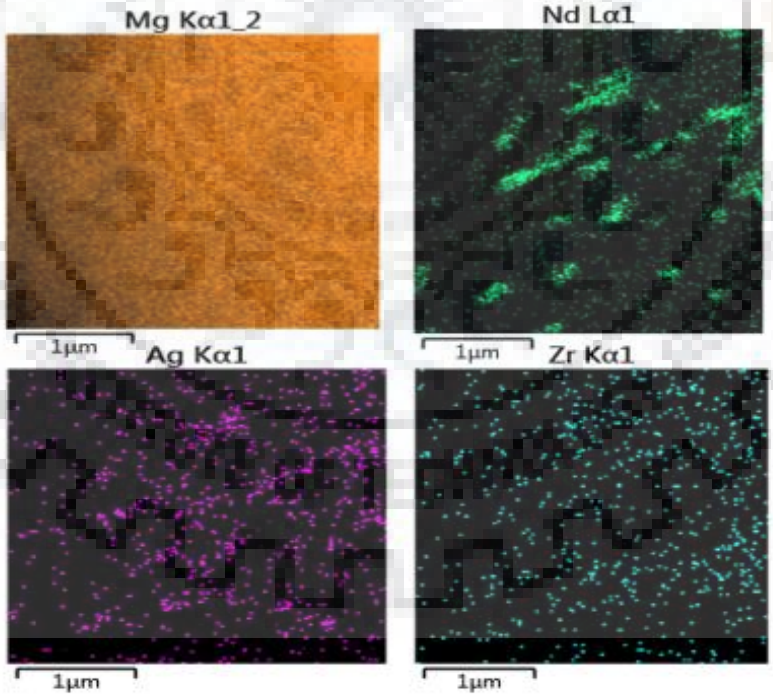

(b)

Figure 23. EDS mapping of (a) as-received, and (b) FSPed QE22 alloy.

7.2. Mechanical properties

Fig. 24 shows the variation of micro hardness across the FSP zone. The distance between the two indentations is 5 mm which is greater than the dimension of the indentation it helps to avoid the effect of strain hardening due to indentation. Hardness increased from 76 VHN for base metal to 90 VHN for the FSP region. The nugget region showed a greater hardness due to increasing the number of grain boundaries, which are responsible for restricting the movement of dislocations. Uniform distribution of fine precipitates ($Mg_{12}Nd$) is also responsible for increasing the hardness of nugget region.

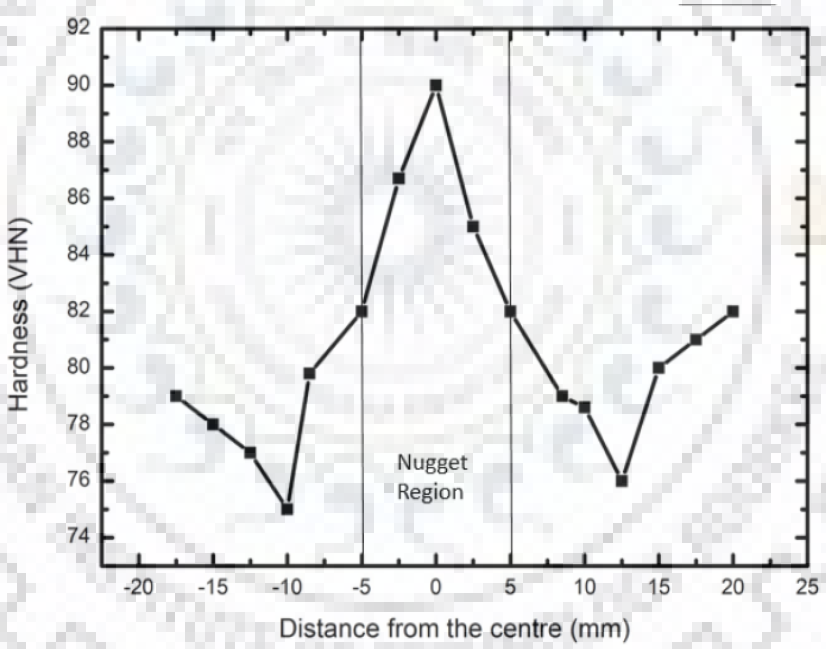

Figure 24. Variation of micro hardness across the nugget zone in friction stir processed QE22 alloy.

7.3 XRD analysis of as-received and FSPed sample

Fig. 25 shows an XRD pattern of both as-received and FSPed sample. XRD peaks are obtained at 1^0/minute scan rate. In Fig. 24 the intensity of some peaks in the FSPed sample is little bit higher or some is lower than that of an as-received sample. These intensity differences are occurs due to change in crystal orientation. Fig. 26 (a) and (b) show the shifting of peaks in rightward direction after the FSPed process due to residual tensile stresses. XRD peaks only show the presence of magnesium in QE22 alloy due to the low weight percentage of alloying elements.

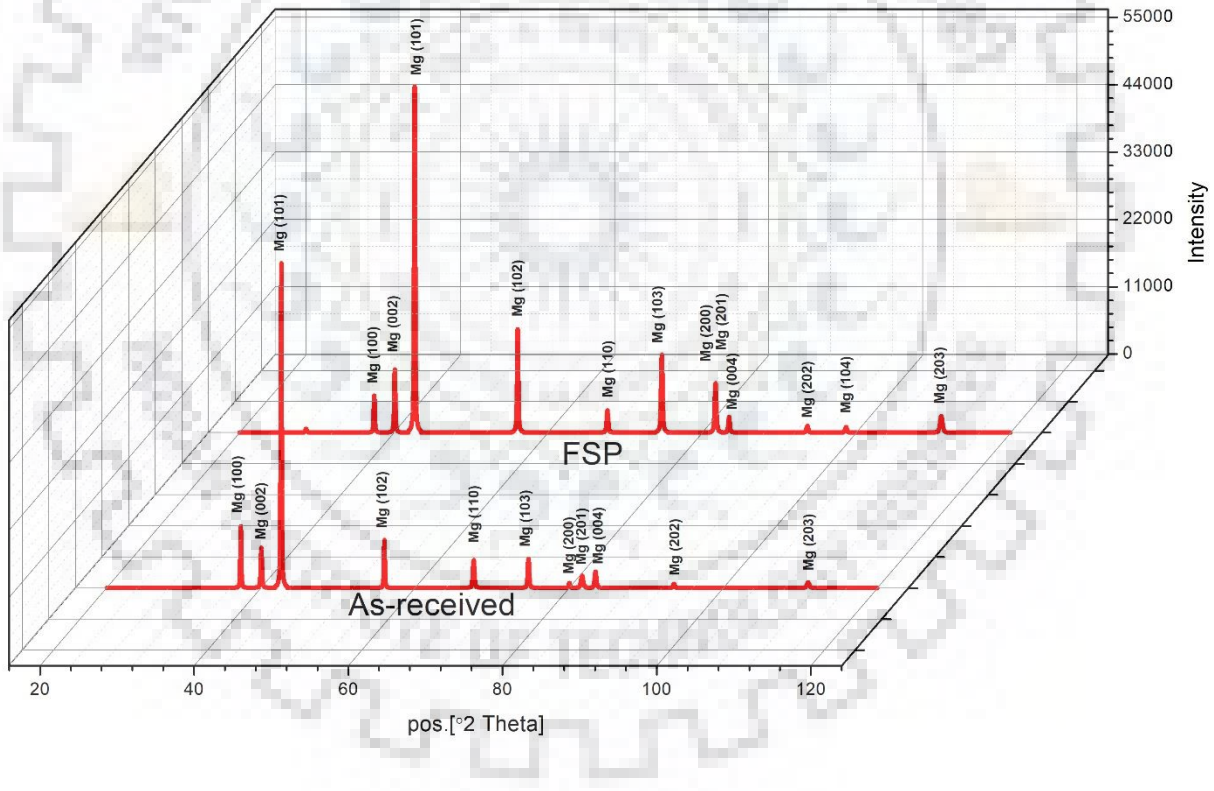

Figure 25. XRD pattern of both as-received and FSPed sample.

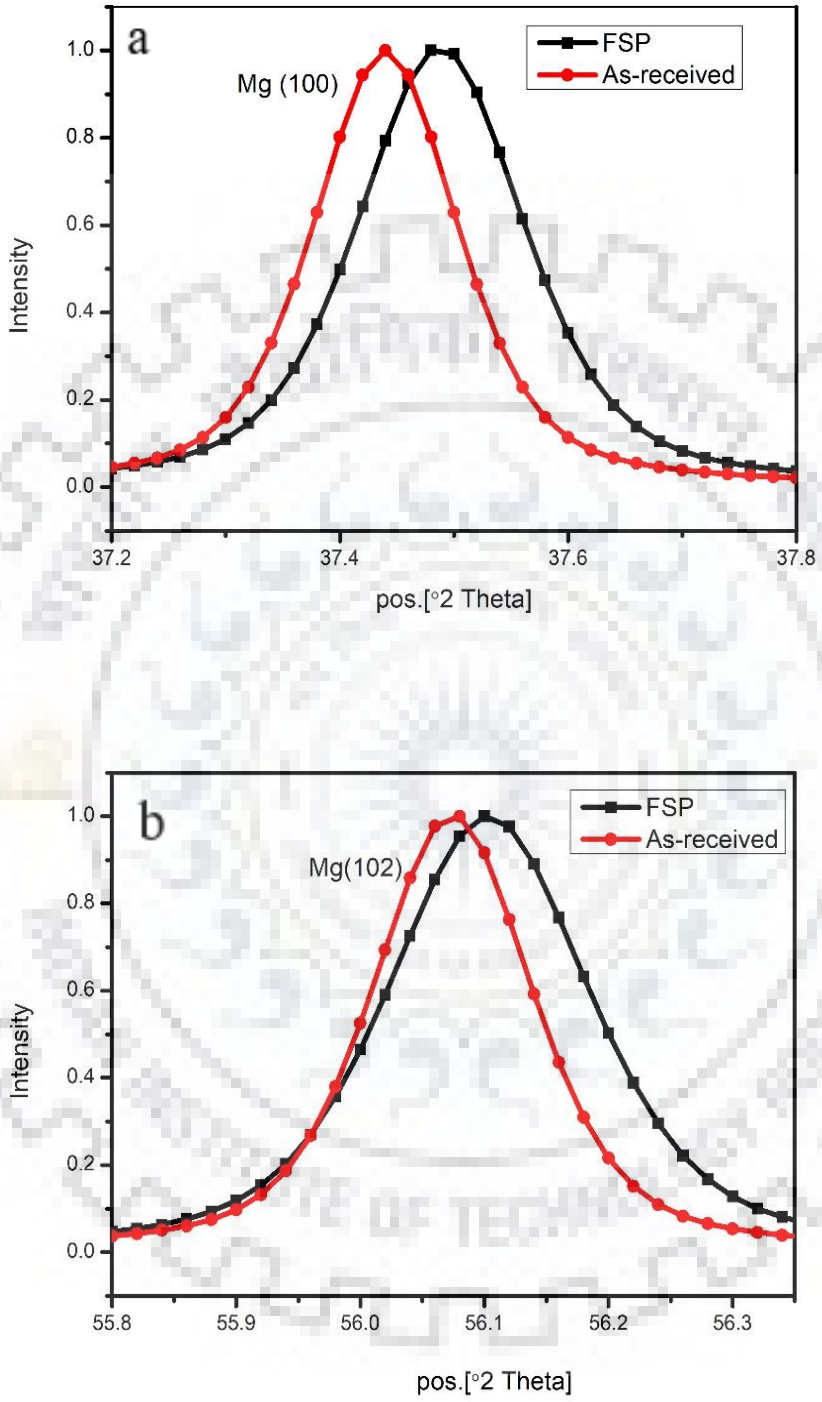

Fig 26. XRD pattern of both as-received and FSPed sample (a) between 37.2^0 to 37.8^0 (b) between 55.8^0 to 56.3^0.

7.4. Open circuit potential

Fig. 27 shows the variation in OCP of FSPed and as received samples over 48 h of immersion time. It shows the variation of electrode potential with immersion time. Large fluctuations are observed in both as received and FSPed sample conditions. Initially, the OCP values of the FSPed sample increased quickly in comparison to as-received sample and the initial OCP values are higher after the FSPed process. However, after 1 h of immersion OCP value of the as received sample is nobler than that of FSPed samples that shows that the anodic dissolution rate in FSPed is more than that of the as received sample. After 10 h there is a rapid fluctuation in the OCP value of as-received sample and it moved towards the nobler potential than that of the FSPed sample. FSPed samples takes minimum time to reach higher OCP values. On the basis of OCP value we can judge the corrosion rate of FSPed and as-received samples. Other tests are required to observe the behaviour of magnesium alloy under corrosive environment.

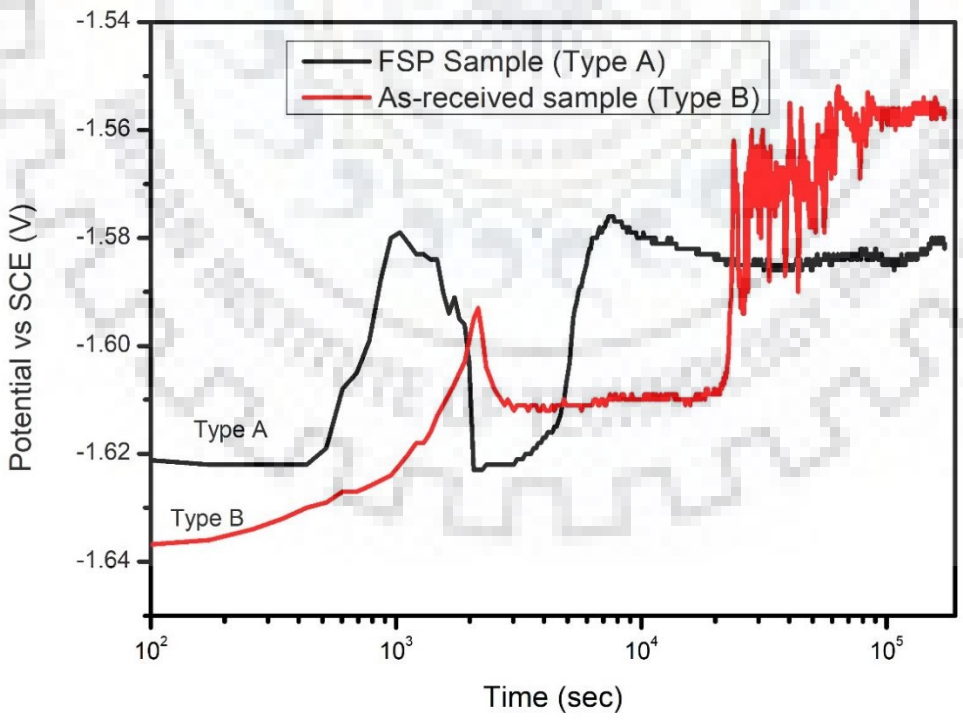

Figure 27. OCP curves of QE22 magnesium alloy in 3.5 wt% NaCl solution.

7.5 Polarization measurements

Fig. 28 shows the potentiodynamic polarization curves of both as received and FSPed QE22 alloys. Stable passive region is not formed in either alloy conditions. The values of corrosion current (i_{corr}) and corrosion potential (E_{corr}) are obtained from Tafel extrapolation. The values of corrosion potential, E_{corr} and corrosion current, i_{corr} are summarized in Table 4. The E_{corr} value of FSPed samples move towards the nobler potential in compare to as-received sample. However, E_{corr} is a thermodynamic parameter that does not represent corrosion kinetics. In Fig. 28, β_a is a slope of anodic polarization curve and (β_c) is a slope of cathodic polarization curve and the value of β_c is greater than β_a, implying that cathodic reactions are responsible for controlling the corrosion rate in both the samples.

The i_{corr} value and therefore the corrosion rate in FSPed samples is greater in comparison to the as received samples. This implies that grain refinement increased the corrosion rate of this alloy. A possible reason is the formation of micro galvanic cells due to increase in the area fraction of refined $Mg_{12}Nd$ phase. Due to this, localised corrosion will transform into uniform corrosion. Another possible reason is micro scale residual stresses during FSP can reduce the activation energy barrier for atoms to leave the lattice and dissolve into the solution. Polarization resistance, R_p, value of as-received sample is higher in comparison to FSPed sample. There is no significant change in the kinetics of cathodic and anodic reactions after grain refinement. Polarization resistance is calculated with the help of i_{corr}, β_a, β_c by using the Stern-Geary equation.

$$R_p = \frac{\beta_a \ \beta_c}{2.3(\beta_a + \beta_c) i_{corr}}$$

Based on this equation, R_p value of as-received sample is more in comparison to FSPed sample.

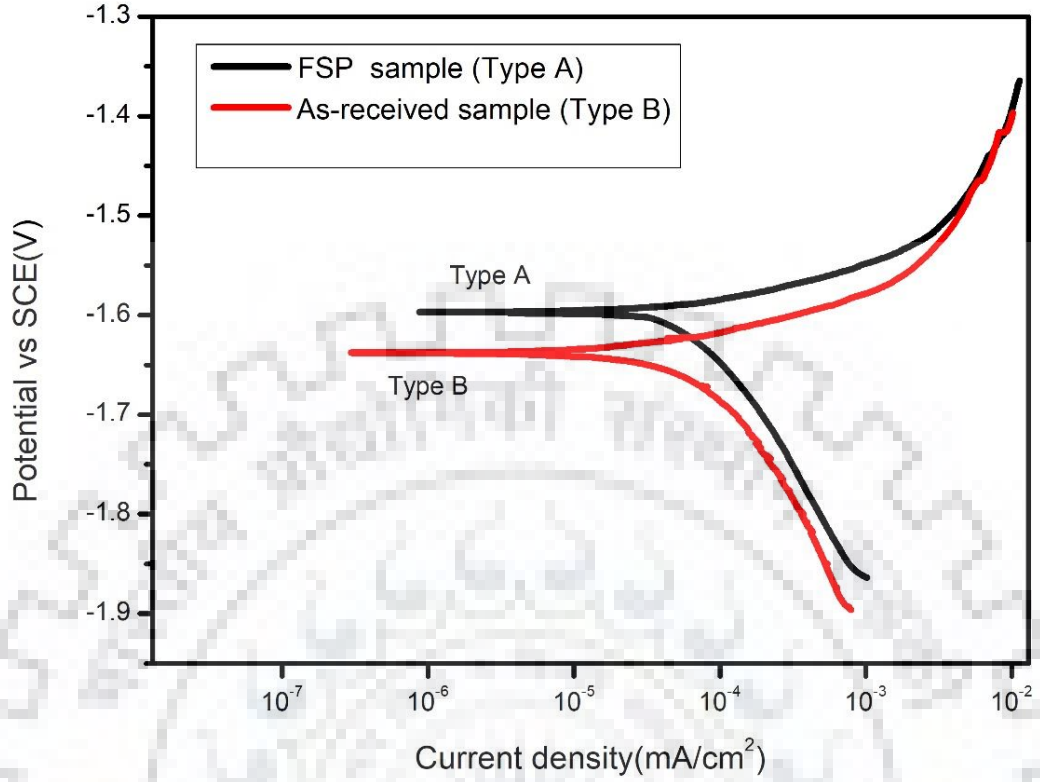

Figure 28. Polarization curves of QE22 alloy in 3.5 wt% NaCl solution.

Table 4. Electrochemical parameters of magnesium alloys in 3.5 wt% NaCl solution.

Sample condition	**E_{corr} (mV vs SCE)**	**i_{corr} (A/cm^2)**	**β_a (mV/decade) vs. SCE**	**β_c (mV/decade) vs. SCE**	**R_p, kΩ. cm^2**
As-received	-1630 ±20	5.5 ±0.4×10^{-5}	40±15	-180±10	0.40±0.03
FSP	-1600±20	8.2± 0.4×10^{-5}	45±15	-220±20	0.296±0.04

7.6. Immersion test

Immersion method is a direct method to estimate the corrosion behaviour of materials. Uniform corrosion rate is directly related to the weight loss during an immersion test. Normalized weight loss per cm^2 after immersion tests is shown in Fig. 29. In initial 1 h, as-received sample exhibited 0.031g lower weight loss as compared to the FSPed sample. In 24 h immersion test, the as-received sample showed 0.011g lower weight loss in compare to the FSPed sample. In 72 h immersion test, the as-received specimen showed about 0.039g lower weight loss in compare to the FSPed sample. In 24h the percentage weight loss in FSPed sample is less in compare to 1h immersion test, which implies that the stacked corrosion products show little protection effect. The pH of the solution after 72 h of immersion testing increased from 7 to 9.2. The increase in pH value of solution occurred by the dissolution of $Mg(OH)_2$ [39]. Fig. 31 shows the SEM images of surface morphologies of QE22 alloy samples before and after immersion test.

There is a significant difference in surface morphologies of FSP and as-received sample. Fewer macroscopic pits could be observed in the as-received sample in 1 h immersion test, but in the FSPed sample large amount of material is removed from magnesium matrix that shows that it corroded more as compared to as-received sample. After 24 and 72 h of immersion test, the pits merged and converted into uniform corrosion [40]. There was a large amount of corrosion product stacked on the surfaces after 24 and 72 h immersion tests. The XRD pattern analysis (Fig. 30) shows that the corrosion product mainly consists of $Mg(OH)_2$. Exactly similar pattern was obtained for corrosion products on the as received QE22 alloy. Due to large number of porosity with cracks in corrosion product $Mg(OH)_2$ it provides less protection [41,42].

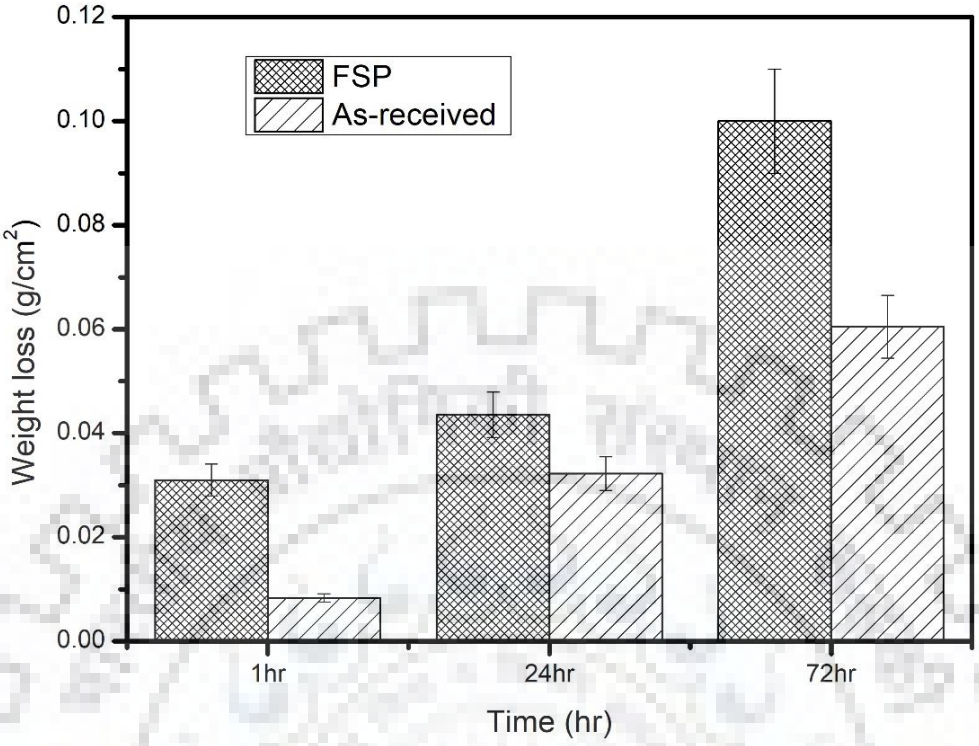

Figure 29. Results of the immersion tests conducted for (a) 1 h (b) 24 h, and (c) 72 h for as-received and FSPed QE22 alloy.

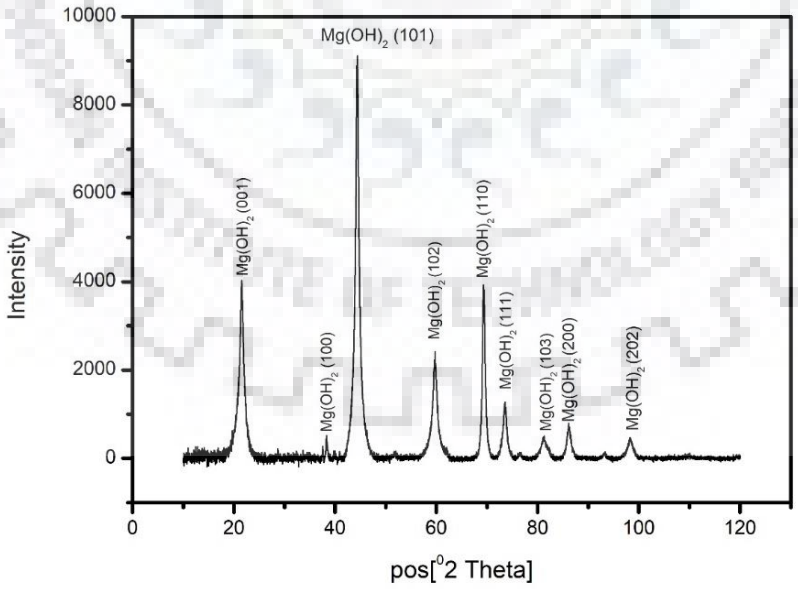

Figure 30. XRD pattern of corrosion product on the surface of FSPed QE22 alloy after 72 h immersion test.

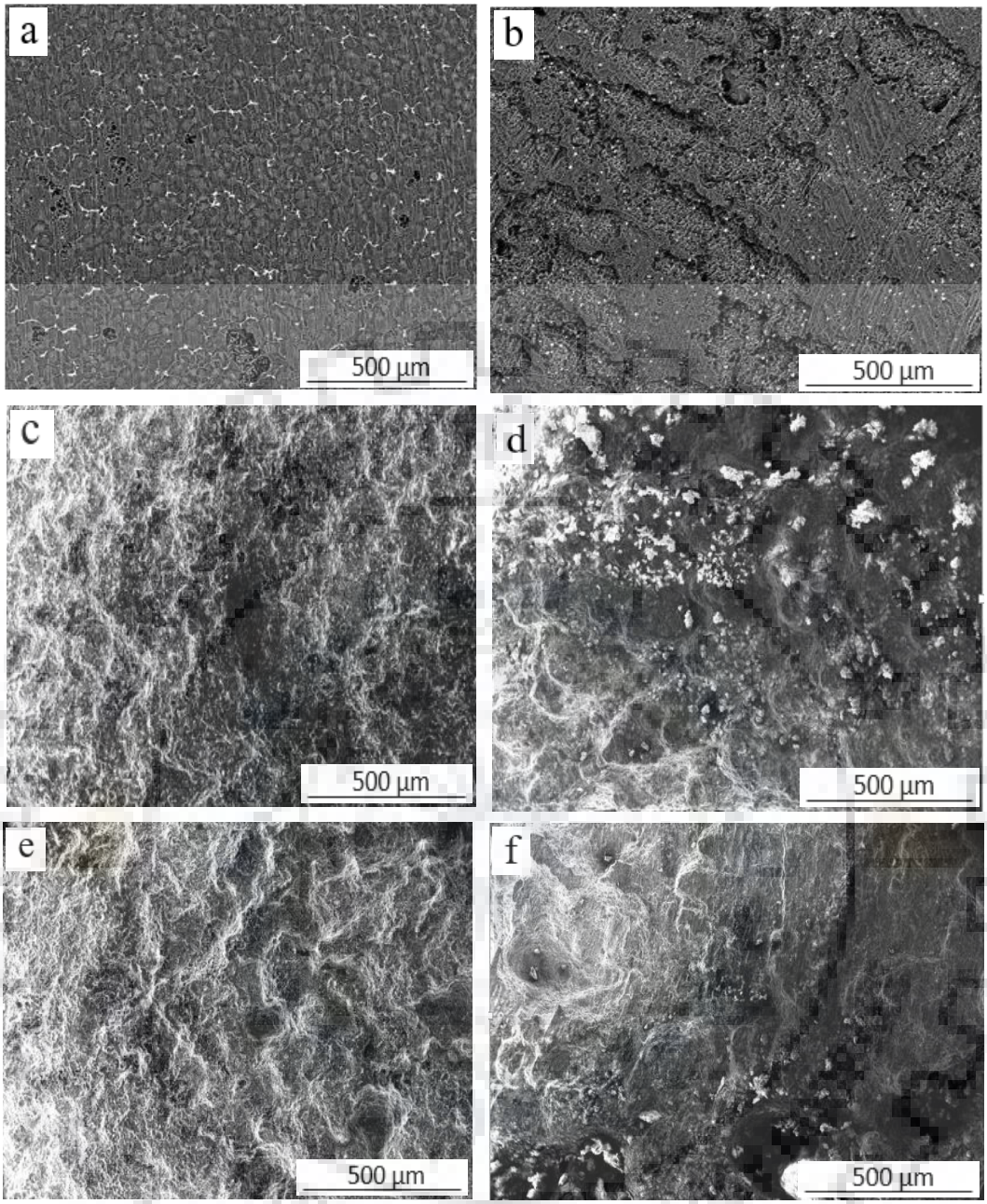

Figure 31. SEM micrographs of (a) as-received alloy after immersion for 1 h, (b) FSPed alloy after immersion for 1 h, (c) as-received alloy after immersion of 24 h, (d) FSPed alloy after immersion of 24 h, (e) as-received alloy after immersion of 72 h (f) FSPed alloy after immersion of 72 h.

7.7 Surface characterization

XPS was performed on the surface of the corroded specimens of as received and FSPed samples to determine the chemistry of surface. XPS spectra obtained from the specimen exposed to 3.5 wt% NaCl solution for 24 h are shown in Fig. 32, 33, 34, 35. Intensity of peaks in FSPed sample is more as compared to as-received sample. Strong signal of $Mg(OH)_2$ can be detected on the specimen surface. In Fig. 33 element silver existed in the form of Ag_2O state and magnesium existed in the form of Mg^{2+} state and along with oxygen in the form of $Mg(OH)_2$ state. In Fig. 34 element zirconium existed in the form of ZrO_2 and neodymium exist in the form of Nd_2O_3. In Fig. 35 element carbon existed in the form of CO_3^{2-} and C-C/C-H state. C1s peaks indicated that the small amount of carbonate present on the specimen surface. It is existed due to the surface contamination during the cleaning action of the specimen [43].

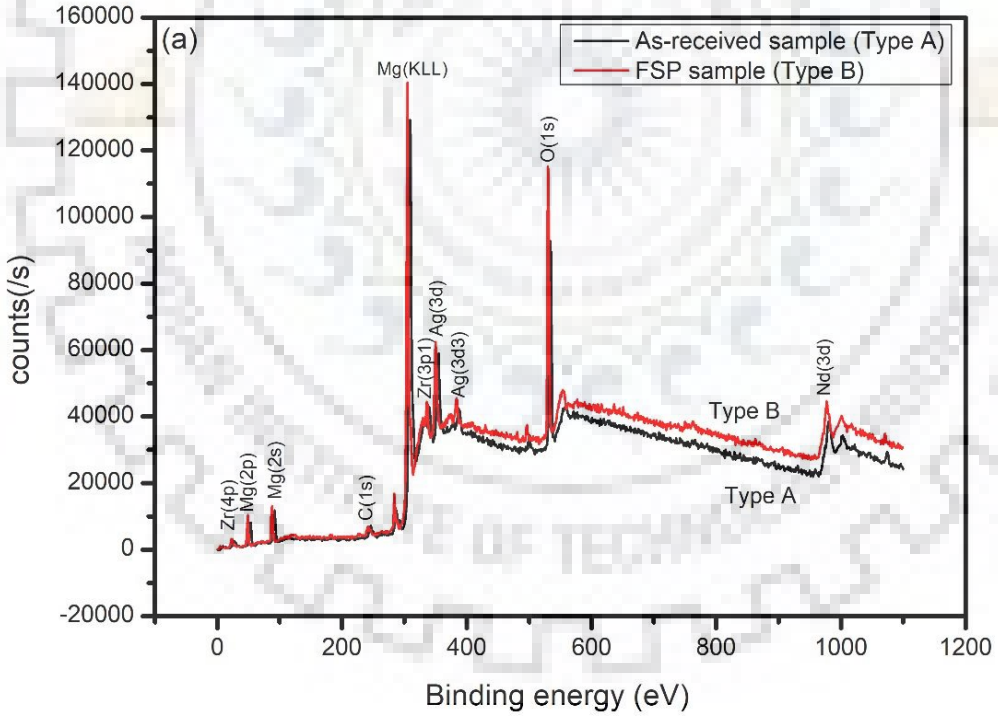

Figure 32. XPS survey curve of both as-received and FSPed samples subjected to 3.5 wt% NaCl solution for 24 h.

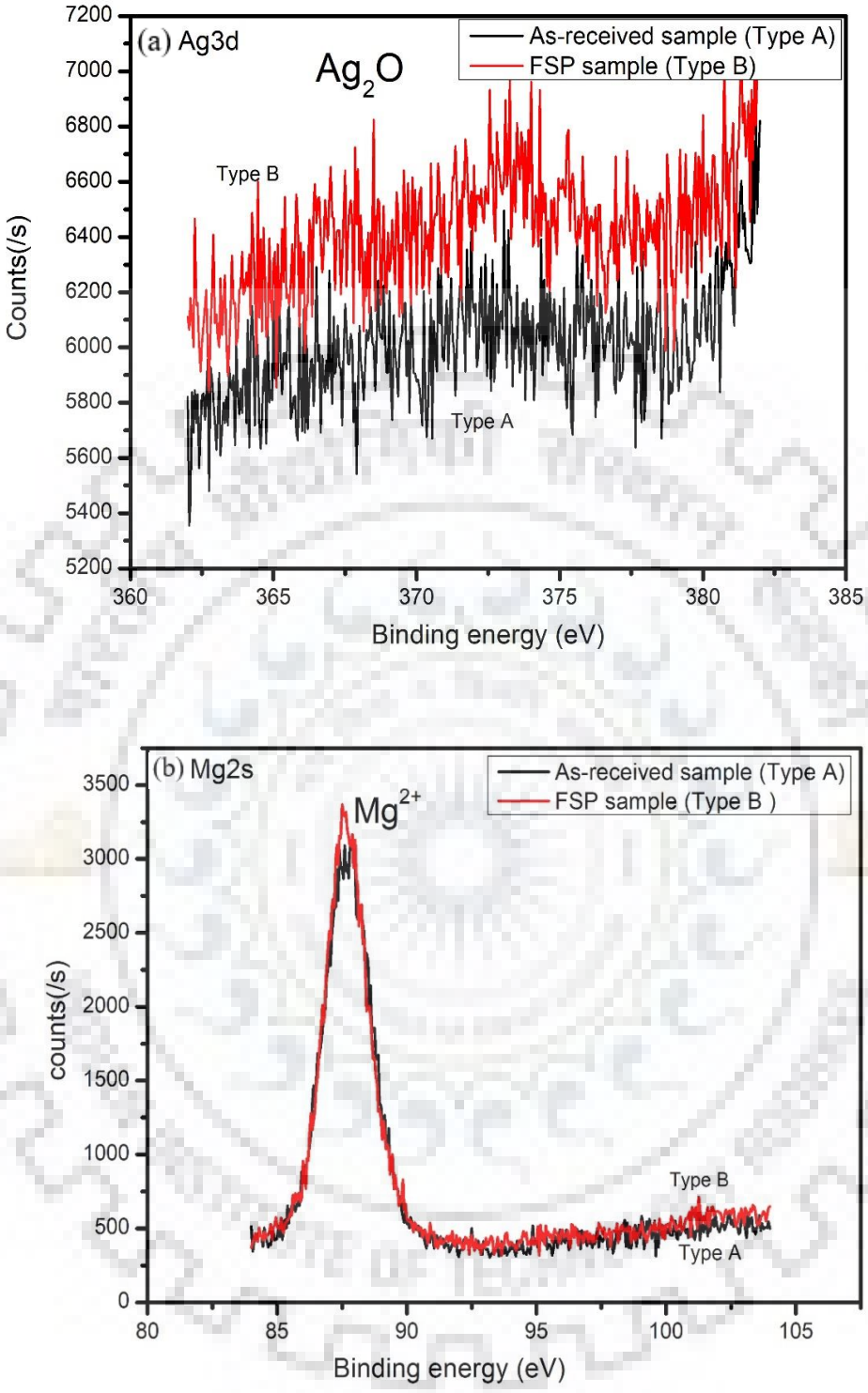

Figure 33. XPS spectra of surfaces on both specimens subjected to 3.5 wt% NaCl solution for 24 h (a) Ag3d, (b) Mg2s.

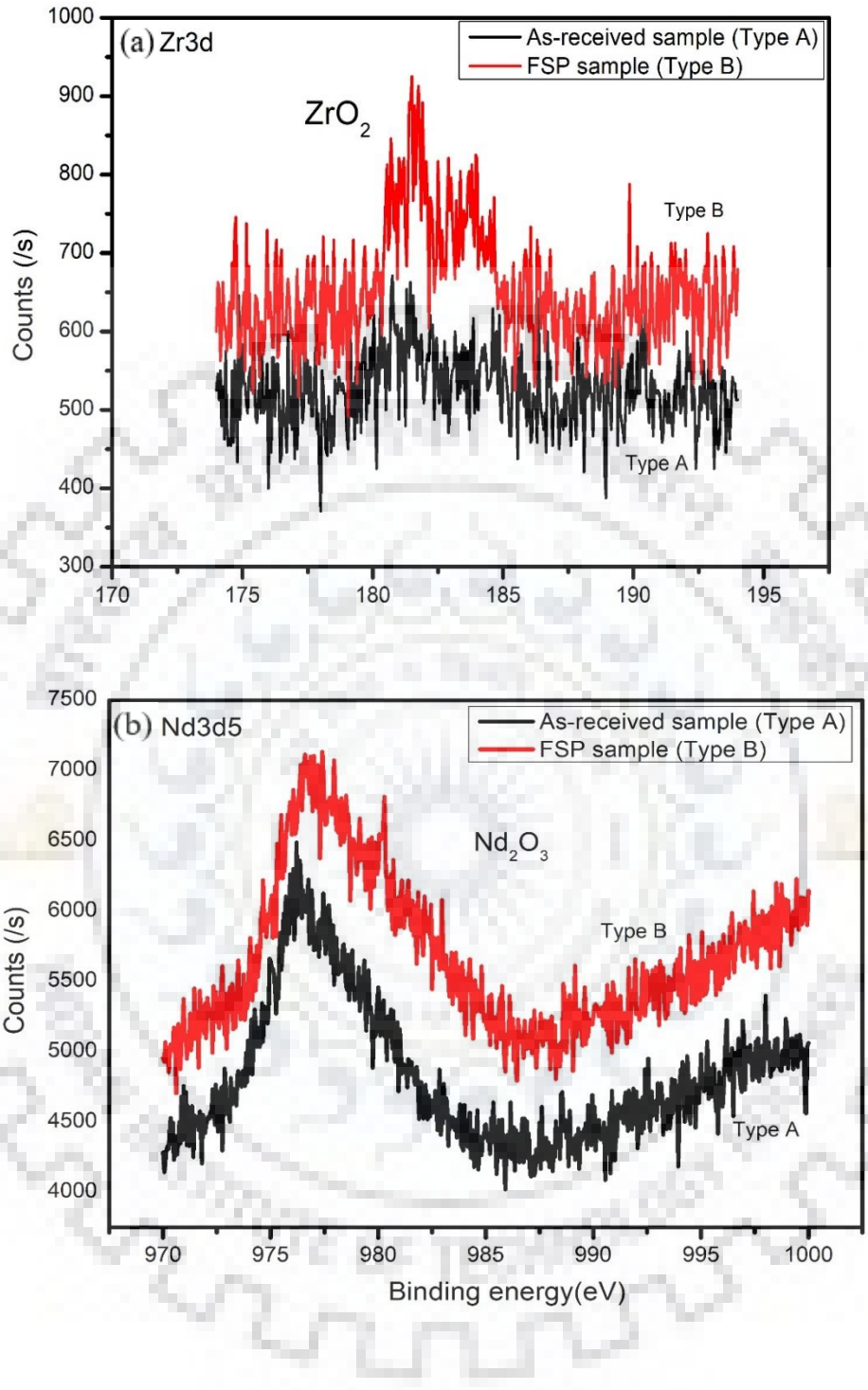

Figure 34. XPS spectra of surfaces on both specimen subjected to 3.5 wt% NaCl solution for 24 h (a) Zr3d, (b) Nd3d5.

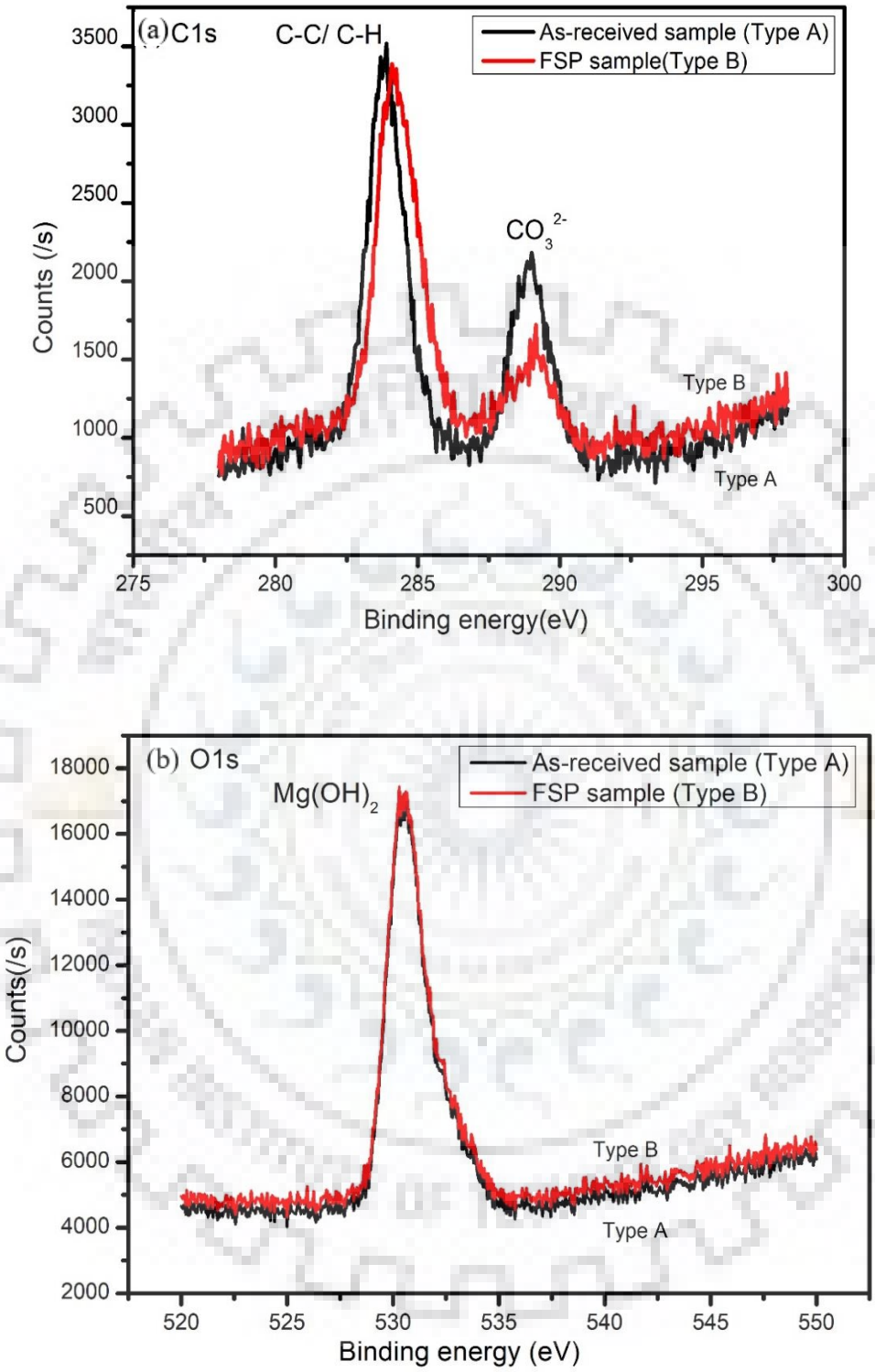

Figure 35.XPS spectra of surfaces on both specimen subjected to 3.5 wt% NaCl solution for 24 h. (a) C1s (b) O1 spectra.

7.8 Electrochemical impedance spectroscopy

EIS tests are performed to detect the change of surface characteristics during the entire immersion period. Fig. 37 shows Nyquist plot of both as-received and FSPed samples after immersion in aqueous solution for different time intervals. Arc of a Nyquist plot is related to metal dissolution rate during the corrosion process in which the diameter of arc is associated with charge transfer resistance [44, 45]. At low frequency, the Nyquist plots reveal a second arc that indicates inductive behaviour of all the samples. However, in our study we neglect the effect of inductance. Two things are revealed from the Nyquist plots of both as-received and FSPed samples. Firstly, the diameter of capacitive arc of FSPed QE22 alloy sample is smaller than that of the as-received sample. Secondly, the diameter of capacitive arc decreased continuously as the immersion time increased indicating a gradual weakening of corrosion resistance.

Fig. 36 shows the equivalent Randle circuit. In circuit, $\mathbf{R_p}$ represents the charge transfer resistance during corrosion reaction, $\mathbf{R_s}$ represents the electrolyte resistance, and $\mathbf{C_{dl}}$ represents the double-layer capacitance or oxide film capacitance. Table 5 summarizes all the elements of Randle circuit from EIS test of alloy samples immersed for different durations. It shows that charge transfer resistance of the as-received sample is higher in comparison to FSPed sample. The corrosion resistance of metals also depends on nature of oxide film [46, 47]. In initial immersion, FSPed samples show higher capacitance compared to as-received sample but after immersion for 6 h and 24 h, the as-received sample shows higher capacitance as compared to FSPed sample. It implies that as-received sample has better corrosion resistance as compared to FSPed sample.

.

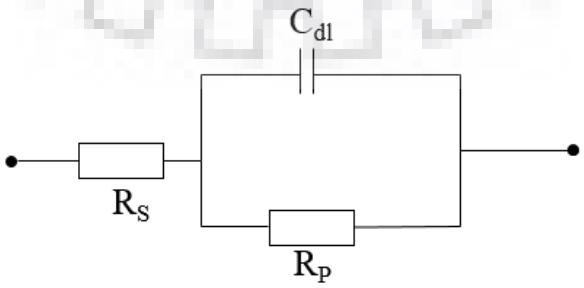

Figure 36. Equivalent circuit of Nyquist plot of as-received and FSPed QE22 alloy samples.

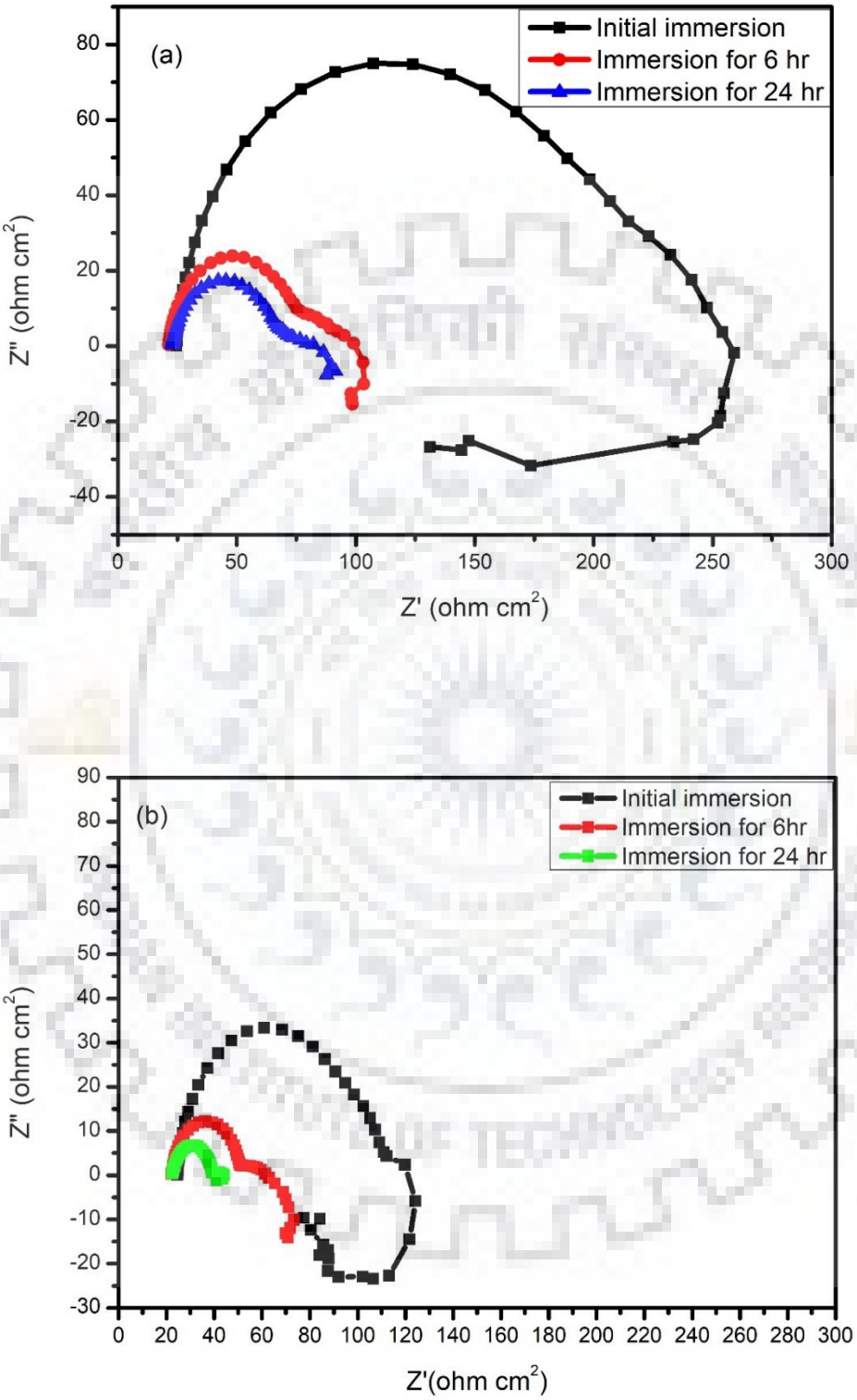

Figure 37. Nyquist plots of impedance spectra of a specimen immersed in 3.5 wt% solution. (a) as-received sample (b) FSPed sample.

Table 5: Results of EIS showing Randle circuit fitting elements for QE22 alloy for different immersion conditions.

QE22 alloy condition	Randle circuit element	Immersion time, h		
		0	**6**	**24**
As received	**R_p (Ohm.cm^2)**	165.3	47.7	33.8
	R_s (Ohm.cm^2)	24.5	22.3	23.5
	C_{dl} faraday/cm^2	309.6 ×10^{-6}	117.5×10^{-6}	105.1×10^{-6}
FSPed alloy	**R_p (Ohm.cm^2)**	65.2	25.7	12.8
	R_s (Ohm.cm^2)	23.9	22. 8	22.7
	C_{dl} faraday/cm^2	338.1×10^{-6}	115.9×10^{-6}	63.72×10^{-6}

7.9. Discussion

The anodic (generation of an electron) and cathodic (consumption of electron) reactions happening during the corrosion of QE22 alloy are given by reactions (2) and (3), respectively. Magnesium hydroxide is formed as per reaction (3).

$Mg \rightarrow Mg^{2+} + 2e^{-}$ (1)

$2H_2O + 2e^{-} \rightarrow H_2 + 2OH^{-}$ (2)

$Mg^{2+} + 2OH^{-} \rightarrow Mg(OH)_2$ (3)

In rare earth added magnesium alloys, the second phase particles have been reported to exhibit noble potential [48]. These precipitates are preferential sites for hydrogen evolution. The overall corrosion morphology depends on the microstructural characteristics, which include (1) size of second phase particles, (2) distribution of second phase particles, (3) grain size of the

matrix, (4) number of crystalline defects. It is reported that grain refinement can improve the corrosion resistance of a material [49, 50]. Copper, titanium, pure aluminium show better corrosion resistance after grain size refinement [51, 52]. However, QE22 alloy after FSP showed poor corrosion resistance in 3.5 wt% NaCl solution. Microstructural characteristics and corrosion mechanism of FSPed samples are associated with this negative phenomena. The corrosion resistance of magnesium matrix depends on the detailed microstructural features like dislocation density, grain boundaries, grain sizes and area fraction of cathodic second phase particles which form micro galvanic cells.

Effect of FSP on the corrosion resistance of QE22 alloy

Surface crystallite defects increases the susceptibility of formation of oxide film [53-54]. Severe plastic deformation converts the microstructure into fine grains which are shown in Fig. 22(a). Deformed QE22 alloy corroded more easily than undeformed as-received sample. Similar phenomena were also found in pure magnesium after ECAP [55]. It is clear that corrosion is accelerated due to the defects like grain boundaries and dislocation [56]. According to this, the stored energy in the deformed grains become easier to be corroded. Along with this there is microgalvanic corrosion due to cathodic second phase precipitate. Together these lead to uniform corrosion, which is shown in Fig. 31. A smaller diameter of a capacitive arc is obtained in the Nyquist plots in FSPed sample, which is illustrated in Fig. 37. The diameter of a capacitive arc is related to the corrosion behaviour of material. More the diameter more will be the corrosion resistance and vice versa. Similar results are found in potentiodynamic polarization tests. The i_{corr} value in FSPed sample is more in compare to as-received sample which is shown in Fig. 28. In immersion tests, more weight loss is found in FSPed sample as compared to as-received sample shown in Fig. 29. So similar trends are found in immersion tests, EIS tests, and potentiodynamic polarization tests. From the above discussion, the factors that weakened the corrosion resistance are- increased the number of micro galvanic cells due to increase in surface area of refined second phase particles, and increase in dislocation density and other crystalline defects due to severe plastic deformation of the material.

From Fig. 27, the OCP values and E_{Corr} values of FSPed samples are nobler than that of as-received samples in initial immersion time period. In the study on corrosion of ECAPed pure magnesium, oxide film in atmospheric air and partial protective film of ($Mg(OH)_2$) in aqueous

solution is related to initial OCP values and E_{Corr}. But still there is no any idea about nature of oxide film. It is expected that the nature of oxide on Mg-Al alloys has a layered structure of MgO/Mg-Al-oxide/substrate [57]. Surface crystalline defects are more prone to the nucleation of oxide film. so the probability of formation of oxide film in FSPed sample would be more which is responsible for shifting the initial OCP value towards the nobler potential. The moment surface contacted with 3.5wt% NaCl solution, a partially protective film of $Mg(OH)_2$ would be formed on the surface. It is expected that the surface film will consist of three layers. The inner layer rich in magnesium, intermediate layer consisting of MgO, and outer layer consists of $Mg(OH)_2$ which is porous in nature [58]. Due to porosity in partially protective films, they provide a poor barrier to penetrate chloride ions into the magnesium matrix [59].

The moment chloride ions reach the surface of magnesium matrix, faster corrosion reaction happens due to enhanced activation of FSPed QE22 alloy. A large amount of hydrogen gas would be produced due to faster reaction kinetics easily breakdown of a partial protective film would happen in compare to as-received sample which can be confirmed by a reduction in OCP values after getting the maximum values as illustrated in Fig. 27. In FSPed samples, surface film is formed quickly as compared to the as-received sample which have similar porosity as that of as-received sample. Similarly, during anodic polarization more fraction of a partially protective film would be formed on FSPed sample due to the crystalline defects as compared to as-received samples. This resulted in nobler E_{Corr} values than that of as-received samples in polarization tests. The moment the applied potential reach the E_{Corr} value, partially protective film of an FSPed sample would break quickly in compare to as-received samples and larger i_{corr} value is obtained.

Effect of second phase particles after FSP on the corrosion resistance of magnesium alloy.

As-received sample has a huge number of second phase particles besides the grain boundaries and triple junction that play two roles- primarily it works as a cathode in the galvanic coupling of QE22 magnesium alloy. Moreover, it works as a corrosion barrier to the corrosion propagation in grains. Second phase is found to be inert in chlorine solution in comparison with magnesium matrix [60]. In the as-received sample, there is a continuous net like distribution of nobler particles ($Mg_{12}Nd_2Ag$) which is shown in Fig. 22 (b) which results in retarded the corrosion propagation in the grains and reduce the corrosion rate. In the assessment of the two contrary special effects of second phase precipitate, micro-galvanic corrosion and corrosion barrier effect [61], the corrosion behaviour of QE22 alloy can be explained. If the second phase is in small fraction it works primarily as a galvanic cathode and accelerates the corrosion of magnesium matrix. If the second phase is in high fraction and there is a net like continuous distribution it works as a barrier against the corrosion propagation in magnesium matrix. In the present work, the FSPed sample greatly changed the morphology of the second phase particles. After FSP process, the second phase precipitates ($Mg_{12}Nd$) are homogenously distributed along the grain boundaries and triple junction in the magnesium alloy. This leads to the formation of a large amount of micro galvanic cells. Another continuous net like precipitates ($Mg_{12}Nd_2Ag$) is dissolved after FSP which is shown in Fig. 22(c). Therefore, two reasons are responsible for increase in the corrosion rate of FSPed sample- (a) formation of a larger number of micro-galvanic cells due to refined ($Mg_{12}Nd$) precipitates, and (b) dissolution of ($Mg_{12}Nd_2Ag$) precipitate, which removed the barrier effect of these precipitates.

Chapter 8

Conclusions and Scope for Future Work

8.1 Conclusions

Fine grained QE22 alloy was obtained through FSP and tests were performed in 3.5 wt% NaCl solution. Effects of microstructure and crystalline defects were analysed.

In QE22 magnesium alloy fine grains are obtained after 2 pass FSP due to sever plastic deformation in comparison to as-received sample. The crystalline defects due to strain induced grain refinement reduce the activation barrier to convert magnesium into its ions and reduced its corrosion resistance. This is evident from higher weight loss in immersion tests, larger i_{Corr} values in Tafle tests, and lesser diameter of Nyquist plot observed in EIS tests.

Due to porous nature of $Mg(OH)_2$ layer partially protective film is formed on the surface of magnesium alloy, as per the enhanced intensities of oxides and hydroxides observed in XPS results. Due to large number of crystalline defects in FSPed sample more fraction of oxide film would be formed and a large amount of hydrogen gas would be produced due to faster reaction kinetics. So breakdown of oxide film would take place rapidly.

Lower corrosion resistance of a plastically deformed QE22 alloy is closely related to the distribution of second phase precipitates. Due to increase in the surface area of ($Mg_{12}Nd$) precipitates resulting from its refinement, number of micro-galvanic cells is increased and due to the dissolution of ($Mg_{12}Nd_2Ag$) precipitates barrier to the corrosion propagation in QE22 is decreased.

Scope for Future Work

Following work can be undertaken in future to explore further in corrosion behaviour of magnesium alloy after severe plastic deformation. Corrosion study on QE22 alloy can be performed after different heat treatments and comparison can be done with respect to morphology and microstructure.

References

[1] K.B. Krauskape, D.K. Bird, Introduction to Geochemistry. New York, NY: McGraw-Hill, 1995.

[2] R.S. Busk, Lattice Parameters of Magnesium Alloys. Trans. AIME. 1950, vol. 188, pp. 1460–1464.

[3] F.W. Von, R.F. Raeuchle., Lattice constants and brillouin zone overlap in dilute magnesium alloys. Physical Review. 1957, vol. 105, pp. 59–61.

[4] A.A. Luo, Recent magnesium alloy developments for automotive power train applications, Mater. Sci. Forum. 2003, vol. 419, pp.57–66.

[5] G.L. Song, Control of biodegradation of biocompatible magnesium alloys, Corros. Sci. 2007, vol. 49, pp.1696–1701.

[6] Z. Yang, J.P. Li, J.X. Zhang, G.W. Lorimer, J. Robson, Review on research and development of magnesium alloys, Acta Metallurgical Sinica (English Letters) 2008, vol. 21, pp.313–328.

[7] M.O. Pekguleryuz, A. Kaya, Creep resistant magnesium alloys for powertrain applications, Advanced Engineering Materials, 2003, vol.12, pp. 866–878.

[8] G.E. Coates, The standard electrode potential of magnesium, Journal of the Chemical Society, 1945, vol. 10, pp. 478–479.

[9] R.Z. Zheng, J. Chen, W. Dietzel, R. Zettler, J.F. Santos, M.L. Nascimento, K.U. Kainer, Corrosion of friction stir welded magnesium alloy AM50, Corros.Sci. 2009, vol.51, pp. 1738-1746.

[10] J.J. Park , L.L. Wyman, Phase relationships in magnesium alloys, WADC Technical Report: Astia Document.1957,vol. 15, pp. 457.-504

[11] M. Drits, E. Padezhnova, N. Miklina, The combined solubility of neodymium and zinc in solid magnesium, Russian Metallurgy.1974, vol.3, pp.143–146.

[12] R. Joseph, K. A. Gschneidner, Solid solubility of magnesium in some lanthanide metals, Transactions of AIME.1965, vol.233, pp. 2063–2069.

[13] A.A. Nayeb , J.B. Clark, The Mg-Nd system(Magnesium-Neodymium), Bulletin of Alloy Phase Diagrams. 1988, vol. 9, pp. 618–623.

[14] S. Delfino, A. Saccone, , R. Ferro, Phase relationships in the neodymium-magnesium alloy system,, Metallurgical Transactions A. 1990, vol.21, pp. 2109–2114.

[15] J. Pahlman, J. Smith, Thermodynamics of formation of compounds in the Ce-Mg, Nd-Mg, Gd-Mg, Dy-Mg, Er-Mg, and Lu-Mg binary systems in the temperature range 650 to 930K, Metallurgical and Materials Transactions B. 1972, vol.3, pp. 2423–2432.

[16] R. Ogren, N.J. Magnani, J.F. Smith, Thermodynamics of formation of binary rare earth-magnesium phases with cesium chloride-type structures, Transactions of the Metallurgical Society of AIME. 1967, vol.239, pp.766–771.

[17] C. W. Bale, P. Chartrand, S. A. Degterov, FT, light Thermochemical Database, CRCT, Montreal, Canada, 2013.

[18] G.L. Song, A. Atrens, M. Dargusch, Influence of microstructure on the corrosion of die cast AZ91D, Corros.Sci. 1998, vol.11, pp.11-33.

[19] K Hanafusa, A. Yamamoto, Y. Katsura, S. Horii, K. Kishio and H. Kumakura, Catalytic effect of silver addition on the low temperature phase formation of MgB_2 superconductor science and technology. 2007, vol.20, pp. 400-410.

[20] D. Song, A.B. Ma, J.H. Jiang, P.H. Lin, D.H. Yang, J.F. Fan. Corrosion behaviour of bulk ultrafine grained magnesium alloy fabricated by equal- channel angular pressing. Corrosion science. 2011, vol.53, pp. 362-373.

[21] M.D. Nave, A.K. Dahle, D.H. St. John, Magnesium Technology. 2000, pp. 243-25.

[22] G. Eddy, J. Poinern, S. Brundavanam, D. Fawcett, A review of material properties, surface modifications and potential as a biodegradable orthopaedic implant American journal of biomedica engineering. 2012, vol. 6, pp. 218-240.

[23] H.S Kim, W.J. Kim, Enhanced corrosion resistance of ultrafine-grained AZ61 alloy containing very fine particles of $Mg_{17}Al_{12}$ phase. Corrosion science. 2013, vol.75, pp.361-364.

[24] Z. Pu, G. L. Song, S. Yang, J.C .Outeiro, O.W. Dillon , D.A. Puleo, I.S. Jawahir, Grain refined and basal texture surface produced by burnishing for improved corrosion performance of AZ31B Mg alloy, Corrosion science. 2012, vol.57, pp.192-201.

[25] H. Bessemer, Improvement in the manufacture of iron and steel, 1865, US Patent No. 49,053.

[26] G.L. Song, A. Atrens, Corrosion mechanism of magnesium alloy, Advanced Engineering Materials. 1999, pp.11-33.

[27] R.C. Zeng, J. Chen, W. Dietzel, R. Zettler, J.F. Santos, M.L. Nascimento, K.U. Kainer, Corrosion of friction stir welded magnesium alloy AM50, Corros.Sci. 2009, vol.51, pp.1738-1746.

[28] M.C. Zhao, M. Liu, G. Song, A. Atrens, Influence of the β-phase morphology on the corrosion of the Mg alloy AZ91, Corros.Sci. 2008, vol.50, pp.1939-1953.

[29] G.M. Hoch, International corrosion conference. National Association of Corrosion Engineers, Houston.1974, vol.3, pp.134.

[30] C.S.Paglia, R.G.Buchheit, Microstructure, microchemistry and environmental cracking susceptibility of friction stir welded, Mater.Sci.Eng.A. 2006, vol.429, pp.107-104.

[31] A. Pardo, M.C. Merino, A.E. Coy, R. Arrabal, F. Viejo, E. Matykina, Corrosion behaviour of magnesium/aluminum alloys in 3.5 wt.% NaCl, Corros. Sci. 2008, vol.50, pp.823–834.

[32] M. Behbahani, P. Najafisayar, M. Pakshir, M. Shahsavari, An electrochemical study on the effect of stabilization and sensitization heat treatments on the intergranular corrosion behaviour of AISI 321H austenitic stainless steel, Corrosion Science. 2018, vol.25, pp.520-532.

[33] M.O. Speidel, M.J. Blackburn, T. R. Beck, J. A. Feeney, Corrosion fatigue chemistry, mechanics, and microstructure of iron based alloy NACE, Houston. 1986, pp.331.

[34] W. S. Loose, Corrosion and protection of magnesium, ASM Int. Materials Park. 1946, pp.173-260.

[35] J.A. Beavers, N.G. Thompson, R. N. Parkins, Stress-corrosion cracking of low strength carbon steels in repository environments. Environmental effects Nuclear and Chemical Waste Management 1985, vol. 5, pp. 279-296.

[36] R. Ambat, N.N. Aung, W. Zhou, Evaluation of microstructural effects on corrosion behaviour of AZ91D magnesium alloy, Corros. Sci. 2000, vol.19, pp.1433-1455.

[37] M. Klein, G. Frieling, F. Walther, Corrosion fatigue assessment of creep resistance magnesium alloy dieMag442 and AE42, Engineering Fracture Mechanics. 2017, vol. 185, pp.33-45.

[38] Priceton Applied Research, Basics of corrosion Measurement, Application Note CORR-1, Oak Ridge, TN 37830.

[39] J.C. Tan, M.J. Tan, Dynamic continuous recrystallization characteristics in two stage deformation of Mg–3Al–Zn alloy sheet**,** Mater. Sci. Eng. A. 2003, vol.339, pp. 124-132.

[40] O. Lunder, J.E. Lein, S.M. Hesjevik, Corrosion morphologies on magnesium alloy AZ91, Mater. Corros. 45 (1994), pp. 331-340.

[41] M.C. Zhao, M. Liu, G.L. Song, A. Atrens, Influence of homogenization annealing of AZ91 on mechanical properties and corrosion behaviour, Adv. Eng. Mater. 2008, vol.10, pp. 93-103.

[42] A.E. Coy, F. Viejo, P. Skeldon, G.E. Thompson, Susceptibility of rare-earth-magnesium alloys to micro-galvanic corrosion, Corros. Sci. 2010, vol.52, pp. 3896-3906.

[43] Z. Liu, Y. Zhu, X. Liu, K.W. Yeung, S. Wu, Construction of polyvinyl alcohol/polylactide glycolide acid nanoparticles on magnesium for enhancing the surface self-antibacterial activity and compatibility of Bio interfaces. 2017, vol.151, pp. 165–177.

[44] C. Cao, On the impedance plane displays for irreversible electrode based on the stability conditions of the steady-state: I. One state variable besides electrode potential, Electrochim. Acta. 1990, vol.35, pp. 831-836.

[45] C. Cao, On the impedance plane displays for irreversible electrode reactions based on the stability conditions of the steady-state: II. Two state variables besides electrode potential, Electrochim. Acta.1990, vol.35, pp.837-844.

[46] Z. Szklarska, S. Mialowska, Mechanism of pit nucleation by electrical breakdown of the passive film, Corros. Sci. 2002, vol.44, pp. 1143-1149.

[47] W.E. Grady, Study of the passive oxide film on iron, J. Electrochem. Soc.1980, vol.127, pp. 555-563.

[48] A.E. Coy, F. Viejo, P. Skeldon, G.E. Thompson, Susceptibility of rare-earth-magnesium alloys to micro-galvanic corrosion, Corros. Sci. 2010, vol.52, pp. 3896-39

[49] A.D. Schino, J.M. Kenny, Effects of the grain size on the corrosion behaviour of refined AISI 304 austenitic stainless steels, Mater. Sci.2002, vol.21, pp. 1631-1634.

[50] M. Janecek, B. Hadzima, R.J. Hellmig, Y. Estrin, The influence of microstructure on the corrosion properties of Cu polycrystals prepared by ECAP, Kovove Materialy. 2005, vol.43, pp. 258-271.

[51] M.K. Chung, Y.S. Choi, J.G. Kim, Y.M. Kim, J.C. Lee, Effect of number of ECAP pass time on the electrochemical properties of 1050 Al alloys, Mater. Sci. Eng. A. 2004, vol.366, pp. 282-291.

[52] A. Vinogradov, T. Mimaki, S. Hashimoto, R. Valiev, Corrosion behaviour of ultra-fine grain copper, Scripta Mater. 1999, vol.41, and pp. 319-326.

[53] G.B. Hamu, D. Eliezer, K.S. Shin, S. Cohen, The relation between microstructure and corrosion behaviour of Mg-Y-RE-Zr alloys, J. Alloys Compd. 2007, vol.431, pp.269-276.

[54] G.L. Makar, J. Kruger Corrosion studies of rapidly solidified magnesium alloys J. Electrochem. Soc. 1990, vol.137, pp. 414-421.

[55] D. Song, A.B. Ma, J.H. Jiang, P.H. Lin, D.H. Yang, J.F. Fan, Corrosion behaviour of equal-channel-angular-pressed pure magnesium in Nacl aqueous solution, Corros. Sci. 2010, vol.52, pp. 481-490.

[56] R.C. Zeng, W. Ke, B.H. Han, Corrosion of artificial aged magnesium alloy AZ80 in 3.5wt% NaCl solution, J.Mater. Sci. Technol. 2007, vol.23, pp.363-368.

[57] G.L. Makar, J. Kruger Corrosion studies of rapidly solidified magnesium alloys J. Electrochem. Soc.1990, vol.137, pp. 414-421.

[58] C.B. Baliga, P. Tsakiropoulos, Development of corrosion resistant magnesium alloys: Part 2. Structure of corrosion products on rapidly solidified Mg–16Al alloys, Mater. Sci. Technol. 1993, vol.9, pp. 513-519.

[59] G. Song, A. Atrens, X. Wu, Z. Bo, B. Zhang, Corrosion behaviour of AZ21,AZ501 and AZ91 in sodium chloride, Corros.Sci. 1998, vol.40, pp.1769-1791.

[60] L.M. Pidgeon, J.C. Mathes, N.E. Woldmen, Corrosion and Protection of Magnesium, ASM International, Materials Park. 1946, vol.20, pp.173.

[61] D. Song, A.B. Ma, J.H. Jiang, P.H. Lin, D.H. Yang, J.F. Fan Corrosion behaviour of bulk ultrafine grained AZ91D magnesium alloy fabricated by equal-channel angular pressing, Corrosion Science. 2011, vol.53, pp. 362-373.